Effect of pre-crack non-uniformity for mini-CT geometry in ductile tearing regime

Meng Li[1,2,*], Rachid Chaouadi[1], Ludovic Noels[3], Inge Uytdenhouwen[1], Marlies Lambrecht[1], Thomas Pardoen[2]

[1]Belgian Nuclear Research Centre (SCK CEN), NMS Unit; Boeretang 200, 2400 Mol, Belgium.

[2]Université catholique de Louvain, Institute of Mechanics, Materials and Civil Engineering (IMMC); Place Sainte Barbe, 1348 Louvain-la-Neuve, Belgium.

[3] University of Liège, Department of Aerospace and Mechanical Engineering ; Allée de la découverte 9, B-4000 Liège, Belgium.

[*]Corresponding author. Email: meng.li1991@outlook.com

ABSTRACT

The mini-CT specimen, as one of the geometries that offers significant advantages, attracts the attention from all over the world for application to fracture toughness measurement. However, one of the shortcomings of this geometry is related to the required tight accuracy of the specimen dimensions, in particular the fatigue pre-crack curvature which often violates the requirements of the ASTM standards. Given the limited thickness of mini-CT geometry, a non-uniform pre-crack tends to develop during fatigue pre-cracking, resulting in a large proportion of mini-CT specimens being considered invalid.

Previous investigations have demonstrated that mini-CT specimens with excessive crack front curvature can still provide meaningful fracture toughness results. In this paper, the effect of pre-crack front non-uniformity on ductile fracture is studied: first, the difference of macro parameters such as the applied load, J-integral and crack tip stress-strain field are investigated to illustrate the varying fracture behavior related to non-uniform pre-crack. Next, two micro-mechanical-based approaches, the Rice-Tracey void growth model and Thomason void coalescence model, are integrated to compare the ductile fracture initiation conditions associated with uniform and non-uniform fatigue pre-crack. Finally, the experimental verification of the ductile fracture simulations is performed for mini-CT specimens with uniform and 30° tilted initial cracks. The results indicate that the pre-crack non-uniformity plays a major role in the redistribution of local J-integral and stress-strain state, further affects the position of crack initiation and the way of crack propagation. Nevertheless, the pre-crack non-uniformity has limited effect on the global properties that are usually expected from fracture toughness tests, such as applied load, J-R curve and

1

30 critical fracture toughness. The requirements in the ASTM E1820 regarding pre-crack front curvature is

31 believed to need to be relaxed.

33

1. Introduction

35 In the context of the structural integrity assessment of nuclear reactor pressure vessels (RPV), one of the

36 most appealing geometry for the determination of the fracture toughness is the miniature compact

37 tension (mini-CT) geometry. This geometry gained increasing interest because of a series of advantages:

38 (1) eight mini-CT specimens can be machined out of one broken Charpy specimen, which provides an

39 effective way to reuse one of the most commonly tested sample, especially under irradiation conditions

40 knowing that available surveillance materials are extremely limited; (2) the cutting method makes

41 specimen reorientation possible, which facilitates the investigation of anisotropic effects; (3) the mini-CT

42 geometry has shown potential to produce meaningful fracture toughness results equivalent to large

43 specimens [1-4].

44 However, although the mini-CT geometry has been proven effective for the direct characterization of

45 fracture toughness, it also imposes some challenges. These challenges are mainly associated with the size

46 effect, which can lead to a deviation in the extracted fracture toughness and subsequently influence the

47 transferability of small specimen data to real component and structures. Additionally, potential technical

48 limitations during the machining of small specimens can result in fully satisfying the ASTM requirements,

49 especially when machining irradiated mini-CT specimens in hot cells. A major potential technical limitation

50 is the increased likelihood of non-uniform pre-crack front development during fatigue pre-cracking, which

51 can be attributed to the reduction of specimen thickness. According to the ASTM standard, when the pre-

52 crack size measured on at least one of the 9 individual points (of the 9 point measurement method)

53 exceeds the $\pm 0.1 \times (b_0 B_N)^{1/2}$ [1] validity limits [5] with respect to the average crack length, the specimen is

54 considered to be invalid. The validity limit is typically more stringent for sub-sized test specimens, as it is

55 directly linked to ligament size and specimen thickness. As a result, a large number of mini-CT specimens

---

[1] b_0 is the original remaining ligament, which is the distance from the original crack front to the back edge of the specimen, that is ($b_0 = W-a_0$). B_N is the net thickness, which is the distance between the roots of the side grooves in side-grooved specimens [5] ASTM, *ASTM E1820-20b*, in *Standard Test Method for Measurement of Fracture Toughness*. 2020, ASTM International: West Conshohocken, PA..

are considered invalid due to excessive pre-crack front curvature, causing unnecessary loss of experimental data. Meanwhile, this also suggests that although the pre-crack front non-uniformity is a general issue for all types of test specimens due to similar amplitude of the variation of the stress state distribution, it does not have a significant effect on the invalid percentage of conventional large CT specimens. Previous research [6] have demonstrated that invalid non-uniform pre-crack front has a very weak impact on the fracture toughness mainly in the brittle fracture regime. Hence, appropriate relaxation could potentially be applied to the apparently too strict pre-crack size requirements in ASTM E1921 [7] for miniaturized geometries in order to efficiently use the "invalid" data.

In this study, the effect of pre-crack non-uniformity is addressed in the context of the ductile fracture regime. The first part of the paper addresses the effect of crack non-uniformity in terms of the macroscopic fracture parameters, in which a comparison is made between mini-CT specimens with uniform and non-uniform pre-cracks. Emphasis will be put on the local mechanical properties in the near tip region that directly control the ductile fracture process, such as local J-integral, stress triaxiality and equivalent plastic strain. The second part of the paper aims at investigating the influence of pre-crack non-uniformity on the initiation of ductile fracture using a simple micromechanics-based model, followed by experimental verification. It is widely acknowledged that ductile fracture in metals is a result of the nucleation, growth and coalescence of voids [8]. Micro-voids nucleate from second-phase particles or inclusions by debonding or fracturing when a critical stress is attained. Once the initial voids are formed, the voids then grow under the action of stress triaxiality and plastic strain. Finally, with the increase of remote plastic deformation, a localization of plastic deformation takes place in the ligament between the neighboring voids [9], the necking of ligament and the coalescence of the neighboring voids follow for small increase of the applied loading. Then, a macroscopic crack forms and further propagates by repeated void coalescence. In this part, firstly, the parameters in the micromechanical model are calibrated based on the experimental data. Subsequently, the critical load and the initiation position of ductile fracture for mini-CT specimens with uniform and non-uniform pre-cracks are determined and compared for the different geometries.

The main objective is to investigate the possible effects that the non-uniform pre-crack may bring by comparing it with an ideal uniform straight pre-crack. The results will be discussed on the possible impact on the requirements in ASTM E1820 regarding the pre-crack front curvature to mini-CT geometry.

2. Experimental program

2.1 Material

The material addressed in this study is the 22NiMoCr37 steel. The chemical composition is given in Table 1. This is a typical RPV steel with 458 MPa yield stress at room temperature (25 °C) and 394 MPa yield stress at 290 °C. The true stress-strain curves obtained from the tensile tests at RT and 290 °C are shown in Figure 1. The mechanical properties deduced from the curves are listed in Table 2. In the generation of the true stress-strain curves, the Bridgman's stress correction [10] was applied to give an approximate true stress at fracture. The corrected fracture stress can be expressed as:

$$\sigma_{F,Bridgman} = \frac{\sigma_F}{\left(1 + \frac{2R}{a}\right)\left[ln\left(1 + \frac{a}{2R}\right)\right]} \tag{1}$$

where a is the minimum radius of the necked section of the tensile specimen, R is the radius of the curvature of the neck. To overcome the difficulty of the measurement of R, a relatively accurate calculation of a/R was proposed by Le Roy et al. [11]:

$$\frac{a}{R} = 1.1(\varepsilon_F - \varepsilon_N) \tag{2}$$

where ε_N is the true strain at the onset of necking, ε_F is the current strain (the true strain at fracture).

Table 1 Chemical compositions (weight%)

Material	C	Si	Mn	S	P	Cr	Ni	Mo	Cu
22NiMoCr37	0.22	0.23	0.88	0.004	0.006	0.39	0.84	0.51	0.08

Table 2 Mechanical properties

Material	T (°C)	E (GPa)	v	σ_y (MPa)	ε_{uts}	σ_{uts} (MPa)	$\sigma_{F,Bridgman}$ (MPa)
22NiMoCr37	25	205.5	0.3	458	0.104	611	1055
	290	189.6	0.3	394	0.11	605	858

T = test temperature, E = Young's modulus, v = Poisson's ratio, σ_y = yield strength, ε_{uts} = uniform elongation, σ_{uts} = ultimate tensile strength.
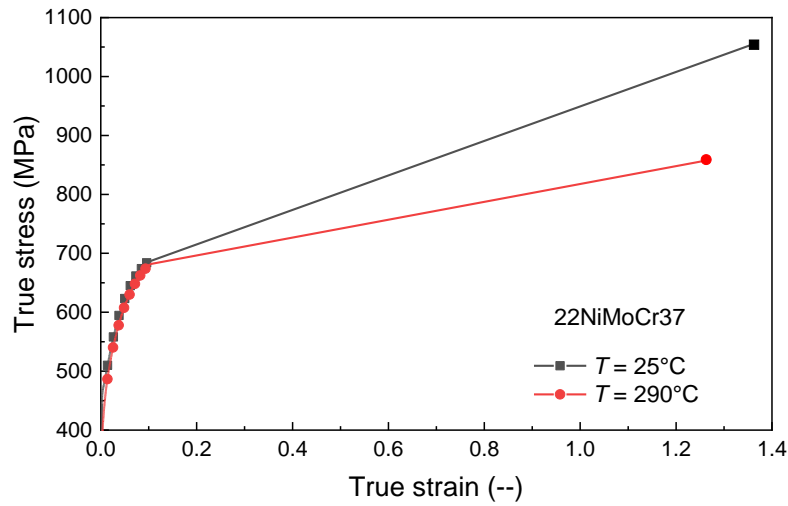
Figure 1 Experimental true stress- true strain curve for the 22NiMoCr37 steel at 25 °C and 290 °C

2.2 Testing procedures

The following fracture toughness tests were performed:

(1) Tensile tests on notched round bar with D_{ext} = 5 mm, D_{int} = 3 mm, notch radius R_{notch} = 1 mm, at room temperature (RT).

(2) Fracture tests on pre-cracked mini-CT specimen with a_0/W = 0.5, W = 8.3 mm, at RT and 290 °C.

(3) Fracture tests at RT on eighteen mini-CT specimens with EDM (electrical discharge machining) machined uniform (tilt angle φ = 0°) and tilted (tilt angle φ = 30°) initial cracks (nine for each crack configuration), with similar dimensions: a_0/W = 0.5, W = 8.3 mm.

The geometries of the round notched tensile specimen and mini-CT specimen are shown in Figure 2, additional dimensions are given in Table 3.

116

117 *Table 3 Dimensions of the specimens*

Specimen			Dimensions			
	T_{test} (°C)	Specimen ID	D_{ext} (mm)	D_{int} (mm)	R_{notch} (mm)	L_{tot} (mm)
Notched round tensile	25	N126	4.886	2.998	0.988	23.961
		N127	4.885	2.990	0.992	23.968
		N128	4.889	2.986	1.018	23.975
		N129	4.876	2.994	0.989	23.968
		N130	4.890	3.000	0.987	23.942
		N131	4.883	2.990	0.987	23.957
	T_{test} (°C)	Specimen ID	W (mm)	B (mm)	a_0 (mm)	B_N (mm)
Mini-CT (fatigue pre-crack)	25	N1	8.253	4.158	3.971	3.299
		N2	8.253	4.128	4.160	3.320
		N113	8.294	4.159	4.153	3.382
	290	N5	8.234	4.179	4.250	3.366
		N6	8.284	4.154	4.240	3.368
	T_{test} (°C)	Crack type	Specimen ID	W (mm)	B (mm)	a_0 (mm)	B_N (mm)
Mini-CT (initial EDM notch)	25	Uniform	N96	8.322	4.169	4.342	3.383
			N98	8.331	4.168	4.273	3.384
			N100	8.334	4.159	4.160	3.379
			N102	8.326	4.159	4.219	3.375
			N104	8.320	4.166	4.196	3.378
			N106	8.330	4.167	4.202	3.371

	N124	8.309	4.166	4.263	3.357
	N125	8.296	4.163	4.237	3.375
	N126	8.292	4.168	4.107	3.380
	N97	8.323	4.163	4.408	3.385
	N101	8.323	4.158	4.205	3.385
	N103	8.324	4.168	4.209	3.399
30° tilted	N105	8.326	4.165	4.238	3.364
	N107	8.320	4.164	4.214	3.379
	N109	8.326	4.173	4.411	3.378
	N127	8.300	4.172	4.271	3.352
	N128	8.286	4.168	4.257	3.389
	N129	8.297	4.172	4.280	3.358

Test group (1) and test group (2) were conducted in an effort to provide a basis for the calibration of the fitting parameters of the micromechanical model, among which, specimen N1 was used additionally to support the verification of the accuracy of the finite element model. The notched round tensile specimens were tested until fracture at test speed 0.2 mm/min at room temperature, following the test method introduced in ASTM E8 [12]. The applied load and the load line displacement were directly measured from the test machine. No extensometer was used during the test, instead, the Digital Image Correlation (DIC) technique was applied to give accurate monitoring and measurements of multiple quantities such as the axial elongation and the diametral contraction in the notch region. The mini-CT specimens were pre-cracked and 20% side grooved, they were tested according to the ASTM E1820 test procedure [5], the crack mouth opening displacement (CMOD) was directly measured using a clip gauge, the crack resistance curves were determined using three techniques to ensure the extraction of robust data: the unloading compliance technique (UC), the normalization data reduction technique (NDR) and the energy normalization technique (EN) [2]. The critical fracture values for tests (1) and (2) are summarized in Table 4. J_Q and $J_{0.2mm}$ are engineering approximations of ductile fracture toughness initiation, J_Q is defined as the intersection of the J-R curve and the 0.2 mm offset line, namely the J value corresponding to 0.2 mm crack extension beyond blunting. $J_{0.2mm}$ indicating the J value corresponding to 0.2 mm absolute crack extension, which plays a role in avoiding the effect of the divergence in the analytical expression of blunting line

136 caused by different standards. In this paper, $J_{0.2mm}$ is considered as the critical toughness corresponding to

137 the crack initiation.

138

139 *Table 4 Measured critical values for ductile fracture*

Specimen			Critical value at crack initiation					
	T_{test} (°C)	Specimen ID	Critical cross section radius (mm)		Critical applied load (N)			
Notched round tensile	25	N126	1.18		4750			
		N127	1.15		4633			
		N128	1.09		4286			
		N129	1.15		4601			
		N130	1.13		4543			
		N131	1.11		4369			
			UC		NDR		EN	
	T_{test} (°C)	Specimen ID	J_Q (kJ/m^2)	$J_{0.2mm}$ (kJ/m^2)	J_Q (kJ/m^2)	$J_{0.2mm}$ (kJ/m^2)	J_Q (kJ/m^2)	$J_{0.2mm}$ (kJ/m^2)
Mini-CT (fatigue pre-crack)	25	N1	440.4	201.5	375.1	210.8	271.8	179.0
		N2	403.3	211.0	344.8	203.2	291.2	193.2
		N113	390.1	204.3	370.6	218.5	333.8	(168.1)[*]
	290	N5	245.3	174.5	231.4	172.0	165.1	(119.6)
		N6	285.9	189.6	217.5	175.0	187.4	(132.6)

140 [*]: data in brackets are excluded due to large deviations.

141

142 The tests in group (3) were conducted to assure the validity of the micromechanics based simulation, and

143 to provide experimental observations on the effect of pre-crack non-uniformity. Since the verification of

144 the simulation results relies on the crack resistance curve and the fracture initiation position, for each

145 initial crack configuration (uniform or tilted), the nine mini-CT specimens were loaded up to different

146 CMOD levels from 0.55 mm to 3.7 mm. The dimensions of the mini-CT specimens were similar in order to

147 minimize their effects on testing results. The results of the test group (3) will be addressed in section 5.4.

3. Finite element procedure

3.1 Finite element model

Finite element simulations were performed using the commercial package ANSYS. Figure 3 shows the finite element models of (a) the notched round tensile specimen and (b) the mini-CT specimen. J2 flow theory based on a power law was assumed for the 22NiMoCr37 steel at RT and 290°C (in section 2.1).

The geometry of the notched round tensile specimen modeled with ANSYS is identical to the real experimental specimen, the analysis of the 1/8 3-D model is enabled due to the symmetry conditions. The displacement was applied at the top surface of the model and symmetric boundaries were applied to the symmetry planes. In order to capture the steep stress-strain gradients, the mesh was highly refined near the fracture region. The half-symmetric model of the mini-CT specimen was 20% side grooved, with initial crack length $a_0/W \sim 0.5$, a symmetric boundary was applied to the remaining ligament plane. The pin to which the displacement is applied was modelled with contact elements to simulate the interaction. The meshing was highly refined in the mean crack tip region. A "spider web" [13] mesh configuration having concentric rings of quadrilateral elements was built, this mesh has proven to efficiently evaluate the J-integral. In the past investigations, it was found that potential effects of the initial crack-tip notch radius on the computed stress state can be considered negligible when the notch radius is small, the initial notch radius which is at least 5 times lower than the CTOD at fracture initiation was proposed [14-16]. However, it should be noted that the distortions of the crack front elements can become unacceptable at higher load level, and the convergence of numerical simulation is significantly affected when the initial notch radius is extremely small, such as a notch radius of $\rho_0 = 0.0025$ mm [17, 18]. Therefore, in this study, in order to ensure the entire loading history of the mini-CT specimen can be analysed, and that accurate results can be generated, the notch radius at the pre-crack tip, ρ_0, was 10 µm (0.01 mm). It can be considered reliable given that it is much smaller than the critical CTOD (0.26 mm).

As specified in the ASTM E1820, the pre-crack front which exceeds the $\pm 0.1 \times (b_0 B_N)^{1/2}$ validity limits [5] with respect to the average crack length is considered to be invalid. As shown in Figure 3, in this study, in order to investigate the effect of pre-crack non-uniformity, the finite element model of invalid non-uniform straight pre-crack with tilt angle $\varphi = 30°$ was utilized to be compared with an ideal uniform straight pre-crack ($\varphi = 0°$). Note that the selected non-uniform crack front is voluntarily exaggerated and real non-uniform crack fronts are much smoother with one or two points, generally close to the specimen surfaces, below the lower validity limit.

(a)

(b)
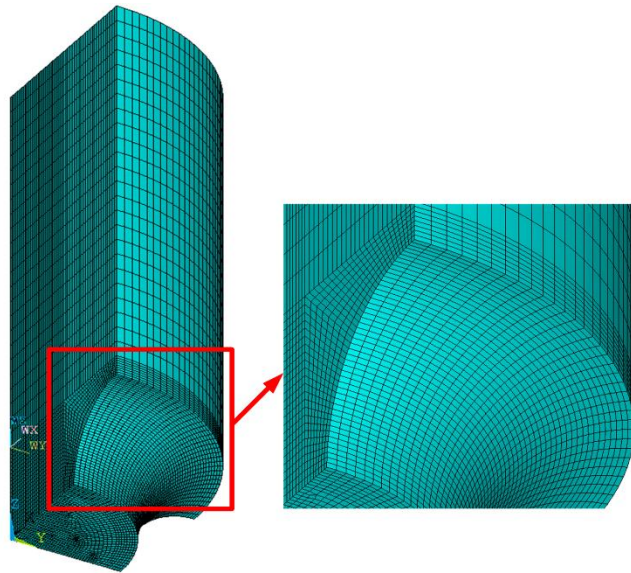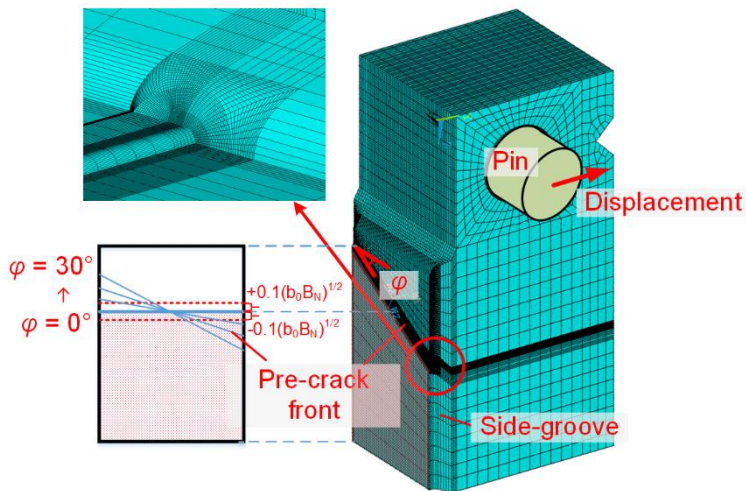
Figure 3 Geometry and finite element model of (a) notched round tensile specimen and (b) mini-CT specimen

3.2 Validation of load and J-integral

The validation of the finite element model was performed by comparing the simulation results (of mini-CT model with uniform pre-crack) with the experimental data (of mini-CT with valid fatigue pre-crack). Following the measurement process in the tests, the applied load was extracted from the pin model, while the CMOD was obtained from the side notch where the clip gage is attached. Figure 4 shows the comparison of the load-CMOD curves obtained from experimental fracture mechanics test and finite

element simulations at room temperature. The simulation results agree well with the experimental data during the crack tip blunting stage before the critical CMOD defined by the 0.2 mm crack propagation. As crack propagation is not considered in this study, this indicates that the model can provide a reliable loading process until crack initiation.

The global J-integral at each loading level was computed by averaging the J values at each of the nodes which are uniformly distributed along the crack front. The local J-integral at each node was evaluated over the contours defined in a plane normal to the crack front, as shown in Figure 5(a), each contour consists of a layer of elements associated with the previous contour. Figure 5(b) compares the J-integral values given by the analytical method and by the numerical method. For the analytical method, the J-integral was computed from the experimental load-CMOD data using the formulae in ASTM E1820 [5]. Note that the mini-CT geometry used at SCK CEN differs slightly from those commonly used in other institutes, which could lead to potential deviations when calculating J-integral using ASTM formulae. However, the deviations are very small. Overall, the simulation results are in close agreement with the ASTM analytical results, before the initiation of ductile fracture.
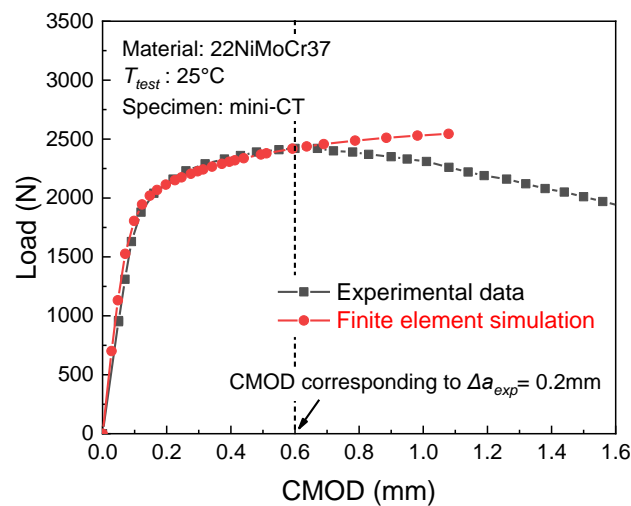
Figure 4 Load versus CMOD curves obtained from finite element analysis and experiments at RT

(a)

(b)
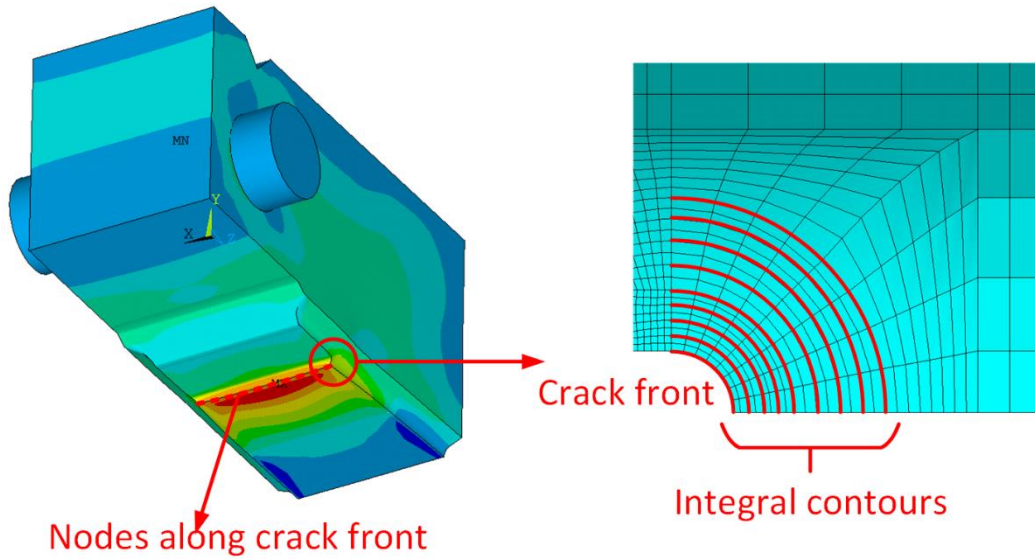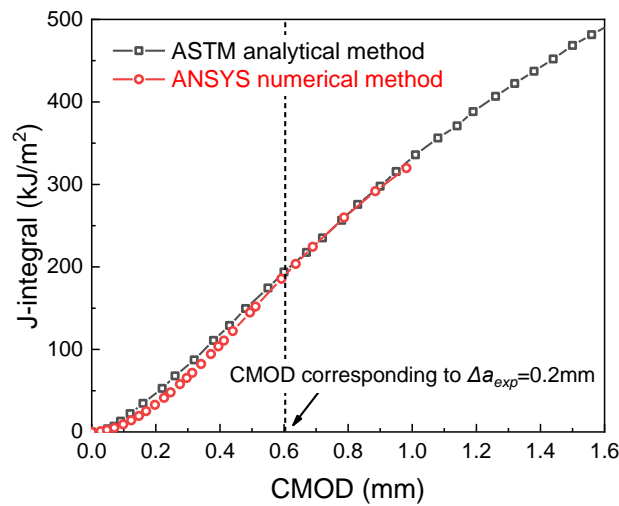
Figure 5 (a) Evaluation method of J-integral (b) J-integral results obtained from ASTM analytical method and ANSYS numerical method

4. Effect of pre-crack non-uniformity on macroscopic parameters

In this section, the effect of crack non-uniformity on macroscopic parameters is analyzed. The numerical investigations mainly focus on the applied load, J-integral and crack tip stress-strain fields for mini-CT specimens with uniform pre-crack front ($\varphi = 0°$) and tilted pre-crack front ($\varphi = 30°$). The crack extension is not taken into account. The flow properties of 22NiMoCr37 steel at room temperature (section 2.1) are applied.

12

4.1 Applied load and J-integral

Figure 6 displays the predicted evolution of applied load with increased CMOD for the mini-CT model with uniform pre-crack front ($\varphi = 0°$) and tilted pre-crack front ($\varphi = 30°$). The good agreement between the two curves indicates the negligible effect of crack non-uniformity on the applied load, the difference in applied load does not exceed 3%.
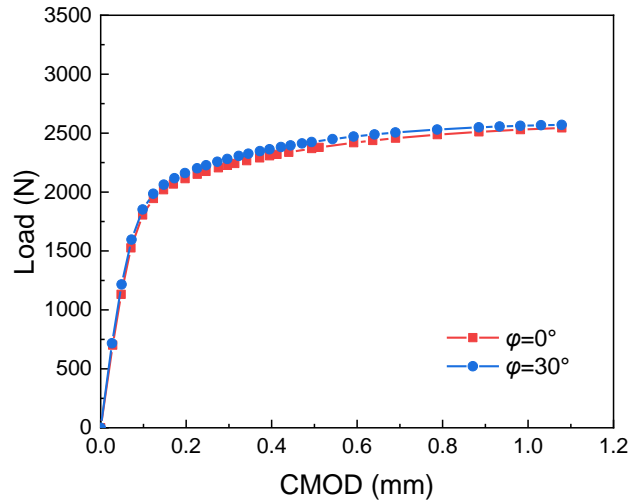

Figure 6 The applied load of mini-CT specimen with uniform and various tilted pre-crack front

Pre-crack non-uniformity effects can be further addressed by looking at the J-integral. Figure 7(a) shows the thickness averaged J-integral (illustrated in section 3.2) generated from mini-CT model with uniform pre-crack front ($\varphi = 0°$) and tilted pre-crack front ($\varphi = 30°$). It is found that before the experimentally measured critical condition of ductile fracture is reached, the two curves are very close to each other. According to the requirements in the ASTM standard, none of the physical measurements of the 9 individual points (9-point measurement method) of initial crack size shall differ by more than $0.1(b_oB_N)^{1/2}$ from the average initial crack length, which corresponds to a validity limit of approximately 13°. The close agreement of the results generated from the two extreme pre-crack configurations ($\varphi = 0°$ and 30°) indicates that the effect of pre-crack non-uniformity on the global J-integral can be considered negligible even if the pre-crack tilt angle exceeds the validity limit. Therefore, in this case, it is not difficult to conclude that for the mini-CT specimens with invalid excessive tilted pre-crack, the global J-integral is hardly affected by the crack front non-uniformity and therefore the *J*-integral calculation method in ASTM E1820 is still applicable.

13

229 More information on the effect of crack non-uniformity can be found in Figure 7(b), where three
230 deformation levels before $J_{0.2mm}$ are taken: J = 100 kJ/m², 150 kJ/m² and 200 kJ/m². The local J-integral over
231 the crack front has a strong dependence on the thickness position, the two pre-crack configurations show
232 significant differences. For the uniform pre-crack, the local J value is maintained at a constant level over a
233 relatively large portion of the crack front center region, and then a lower J value is found near the free
234 surfaces as the plane stress condition is achieved. At larger deformation levels, the distribution of local J-
235 integral becomes more uniform over a moderate to large portion of the crack front (1 mm~ 3 mm), the
236 drop of the local J value approaching the two free surfaces becomes more obvious. For the tilted pre-crack,
237 the local J value increases from a minimum value on the side with the deep pre-crack to a maximum value
238 close to the side with the shallow pre-crack, then followed by an immediate drop. The curves are less
239 uniform across the entire specimen thickness range, and the maximum J value is larger than that on the
240 uniform pre-crack front at the same deformation level. Therefore, the tilt angle of the pre-crack front
241 redistributes the local J-integral variations along the crack front instead of affecting the evolution of the
242 global J-integral value.

(a)

(b)
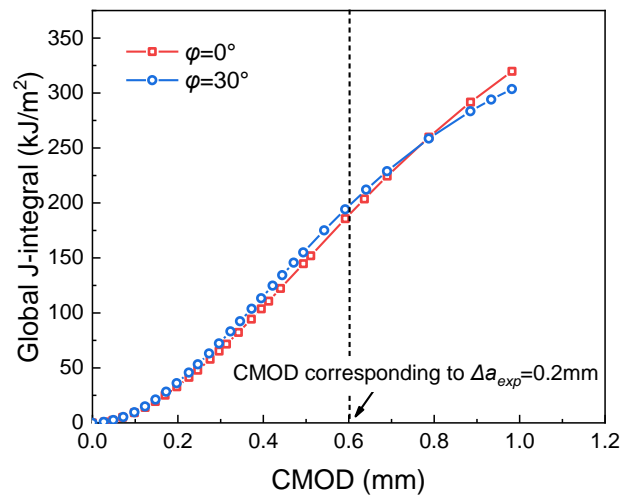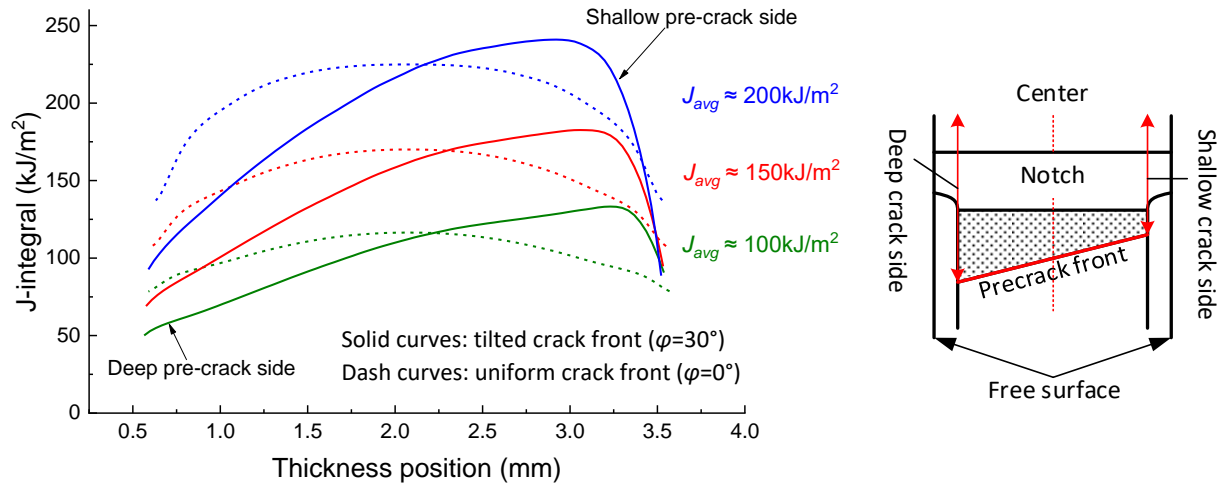
Figure 7 (a) The global J-integral of mini-CT specimen with various pre-crack front (b) The local J-integral distribution along uniform and tilted pre-crack front

4.2 Crack front stress triaxiality and equivalent plastic strain

The stress triaxiality (the ratio of hydrostatic stress and Von Mises equivalent stress) and equivalent plastic strain ahead of the crack front are investigated to better understand the effect of the crack non-uniformity. Figure 8 shows the maximum stress triaxiality as a function of the J-integral. First of all, it is important to realize that the mini-CT geometry tends to experience a loss of constraint no matter what uniformity of the crack front. The maximum stress triaxiality on the ligament plane decreases at an early stage of loading, which is followed by the large scale yielding condition. In order to minimize the effect of the vanishing of the J-dominated zone caused by the large scale yielding condition, a comparison is made at the J level of 20 kJ/m^2, which corresponds to the small scale yielding condition (SSY).

2.8
2.6
2.4
2.2
2.0
1.8
1.6

Maximum stress triaxiality (--)

20kJ/m^2

0   50   100   150   200   250
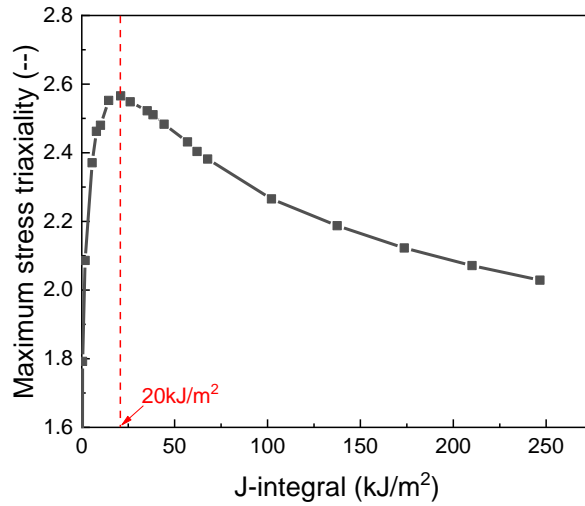
J-integral (kJ/m^2)

Figure 8 Variation of maximum stress triaxiality with J-integral
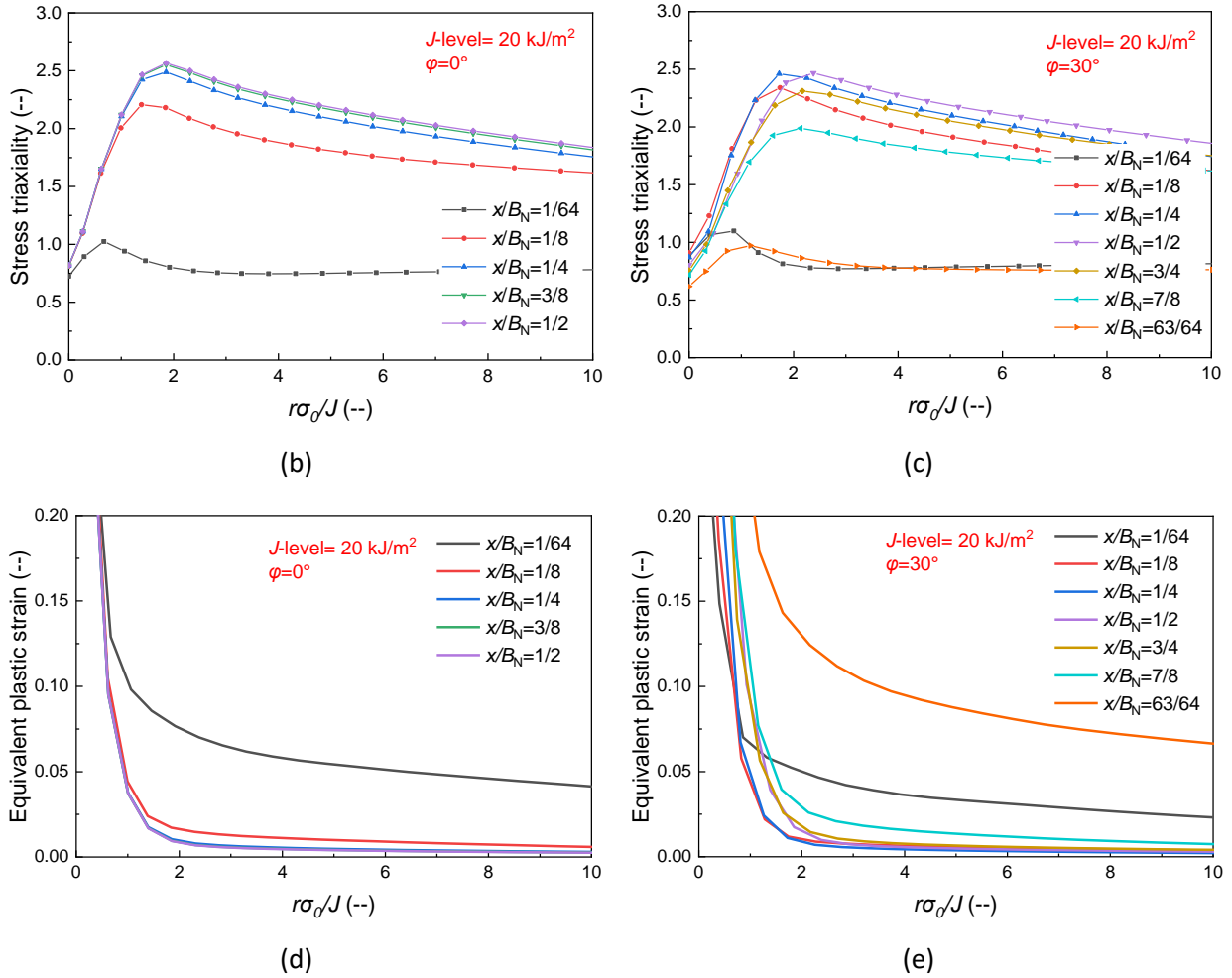
Figure 9(a) shows a schematic drawing of the thickness positions in the uniform crack front (left) and the tilted crack front (right). Figure 9(b-e) give the distribution of stress triaxiality and of the equivalent plastic strain at various thickness positions for a *J*-level of 20 kJ/m^2(see Figure 9-a) in front of uniform and non-uniform pre-cracks. The distance to the crack tip (*r*) is normalized by the ratio of the J-integral and the material's yield strength, J/σ_0. The results reveal that the distribution of stress triaxiality and of equivalent plastic strain are clearly affected by the tilting of pre-crack front. For the uniform pre-crack, the distributions of the parameters are symmetric, the maximum stress triaxiality near the mid-thickness position ($1/8 \leq x/B_N \leq 1/2$) is more than twice as large as that near the side surface as a result of plane stress condition (see Figure 9-b), the equivalent plastic strain is significantly larger near the side surface (see Figure 9-d). For the 30° tilted pre-crack front, the distribution of the stress triaxiality and equivalent plastic strain contrast with those for the uniform pre-crack. Indeed, they are partially similar in the sense that the considerably larger stress triaxiality is still maintained at the positions close to the mid-plane of the specimen ($1/8 \leq x/B_N \leq 7/8$) over the range $1.7 \leq r\sigma_0/J \leq 5$ (see Figure 9-c), and the maximum stress triaxiality for both crack configurations are comparable (≈ 2.5). However, due to the geometry of the tilted crack configuration, each node on the crack front experiences a different local driving force, thus resulting in a stress-strain field that is not symmetrical about the mid-thickness plane. The maximum stress triaxiality is observed to be located at the portion of crack front between the thickness position $x/B_N = 1/4$ and $x/B_N = 1/2$. For the two sets of positions symmetrical about the mid-thickness plane, the position $x/B_N=1/8$ and 1/4 (near the side with deep pre-crack) has slightly larger stress triaxiality than that at the position $x/B_N =$

275 7/8 and 3/4 (near the side with shallow pre-crack) respectively. Then attention is given to the distribution

276 of equivalent plastic strain ahead of the tilted pre-crack front (see Figure 9-e). The distribution is broadly

277 consistent with that shown in Figure 9(d), the equivalent plastic strain is maintained at a relatively lower

278 level over a large fraction of the specimen thickness ($1/8 \leq x/B_N \leq 3/4$), lower than 2% over the distance range

279 $r\sigma_0/J \geq 2$. By contrast, the effect of the tilting angle appears largely in the equivalent plastic strain close to

280 the two side surfaces. Due to the earlier deformation, a significantly larger equivalent plastic strain value

281 can be observed on the portion of crack front close to the side with shallow pre-crack ($x/B_N = 63/64$), the

282 strain is around 2.5 times larger than that on the other side ($x/B_N = 1/64$). Similarly, the equivalent plastic

283 strain at the thickness position $x/B_N = 7/8$ is also raised to around 2.5 times larger than that at the centrally

284 symmetrical position $x/B_N = 1/8$.

285 Apparently, the difference exhibited by stress triaxiality and equivalent plastic strain indicates a clear effect

286 of the crack non-uniformity. Besides, it also provides an interesting case for the investigation on the impact

287 of crack non-uniformity on the ductile fracture initiation. According to the previous research [19-21], local

288 fracture criterion requires the attainment of a critical value governed by both stress triaxiality and plastic

289 strain to trigger ductile fracture. As observed from the existing experiments, the fracture usually initiates

290 in the central part of a quasi-uniform crack front. Whereas for the tilted crack configuration under

291 consideration, the initiation state may vary due to the redistribution of stress triaxiality and equivalent

292 plastic strain along the crack front. However, the absence of a local fracture criterion at this stage makes

293 it difficult to quantify. A model with solid physical basis that takes the effect of both stress triaxiality and

294 plastic strain into account should be considered. In the following sections, a simple micromechanical-based

295 model that is capable of characterizing the process of the void growth and the void coalescence is adopted

296 to compare the two pre-crack configurations (φ=0° and 30°), thus providing additional support to the study

297 on the effect of pre-crack non-uniformity.
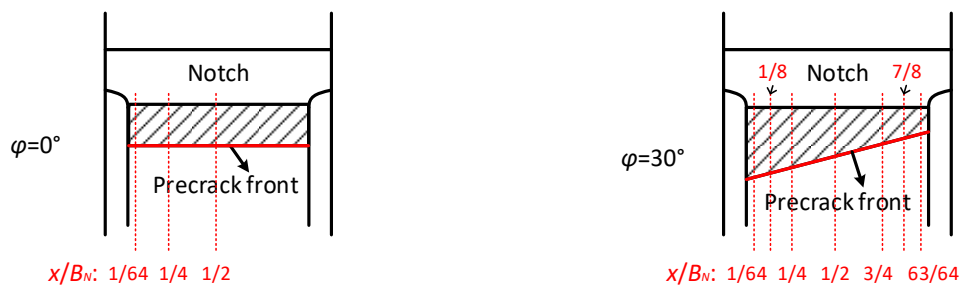
(a)

(b)

(c)

(d)

(e)

5. Effect of pre-crack non-uniformity on the initiation of ductile fracture

5.1 Micromechanical-based models of ductile fracture

303 Prior research has demonstrated that a micromechanical approach can provide an effective simulation of

304 the void nucleation, void growth and void coalescence of ductile fracture under varying conditions of

305 constraint [8]. In this paper, for the simulation of RPV steels, the void nucleation is neglected, the void

306 growth and void coalescence are assumed to be the dominant mechanisms of the damage process. Two

307 models are applied: the Thomason void coalescence model is used to simulate the onset of void

308 coalescence, and then characterizes the initiation of ductile fracture with the help of an additional

309 parameter - the characteristic length. The Rice-Tracey void growth model is used to estimate the void size

310   parameter in the void coalescence model which characterizes the void enlargement evolution before the

311   localization occurs. It should be noted that, although the micromechanical-based model is simple, the

312   motivation for using this model lies in its ability to take into account the effects of both stress triaxiality

313   and plastic strain on ductile fracture. Instead of providing accurate predictions which are not available and

314   outside the scope of the present work, the micromechanical-based model is used mainly for the aim of

315   providing a simple and fundamental way to compare the fracture initiation of two pre-crack configurations.

316   5.1.1 Rice-Tracey void growth model (R-T model)

317   Before the coalescence of microvoids, the ductile fracture is dominated by the void growth. Some early

318   contributions on the growth rate of microvoids made by McClintock [22] and Rice and Tracey [23]

319   demonstrated that the void growth is mainly dependent on the magnitude of the stress triaxiality and of

320   the equivalent plastic strain:

321
$$\frac{dR}{R} = \alpha e^{1.5T} d\varepsilon_{eq}^{p} \tag{3}$$

322   where ε_{eq}^{p} is the equivalent plastic strain; T is the stress triaxiality which is defined as the ratio of

323   hydrostatic stress and Von Mises equivalent stress, $T = \sigma_m/\sigma_{eq}$; dR/R is the growth rate of microvoids.

324   In the later study of Huang [24], the dilatation rate factor α was modified to 0.427 (initially α = 0.283),

325   which dedicates a 50% increase of accuracy.

326   5.1.2 Thomason void coalescence model

327   The void growth process is interrupted by the onset of void coalescence. At the onset of void coalescence,

328   the plastic flow starts to localize inside the ligament between the microvoids, while the material other

329   than the ligament region unloads elastically [8], the initiation of fracture therefore proceeds. The onset of

330   the void coalescence occurs when the normalized maximum axial stress, σ_{max}/σ_0, reaches the critical load

331   defined by $I(\chi)$, where σ_0 is the yield stress of the material. A model proposed by Thomason [25, 26] to

332   describe this process can be expressed as:

333
$$\frac{\sigma_{max}}{\sigma_0} - I(\chi) \geq 0 \tag{4}$$

334   Where $I(\chi)$ is the critical damage factor whose value depends on the microstructure of the material:

335
$$I(\chi) = [1 - \chi^2]\left[\alpha\left(\frac{1-\chi}{\chi}\right)^2 + \beta\chi^{-\frac{1}{2}}\right] \tag{5}$$

336   where χ is the relative void spacing (void ligament size ratio), $\chi = R_r/L_r$ (see Figure 10). α and β are two

337   constants which depend on the value of strain hardening exponent n, following the research of Pardoen

338   and Hutchinson [16], α and β are defined as $0.1+0.217n+4.83n^2$ and 1.24 respectively, for $0 \leqslant n \leqslant 0.3$.

339   As shown in equation (5), χ is the dominant controlling parameter of the onset of void coalescence, $\chi =$

340   R_r/L_r can be written as:

$$\chi = \frac{R_r}{L_r} = \frac{R_r}{R_0} \frac{R_0}{L_{r0}} \frac{L_{r0}}{L_r} \qquad (6)$$

342   where subscript "r" indicates the direction normal to loading (see Figure 10), subscript "0" indicates the

343   initial values. R_r and L_r are the dimensions of the void and the representative volume element in the r

344   direction. $R_0/L_{r0} = \chi_0$ is the relative initial void spacing, which is related to the initial porosity and initial

345   void shape [8]. L_{r0}/L_r is the deformation of the representative volume element in the r direction. In this

346   study, the focus is mainly on the loading stage before crack initiation, due to the limited voids elongation

347   at crack tip at this stage, an approximation $R_r = R_z$ (R_z is the dimension of the void in the direction

348   parallel to loading) during the loading of specimen is assumed. Therefore, R_r can be expressed as the

349   radius of the void after deformation, and R_r/R_0 is the ratio of current void radius and initial void radius,

350   which can be computed using R-T void growth model.
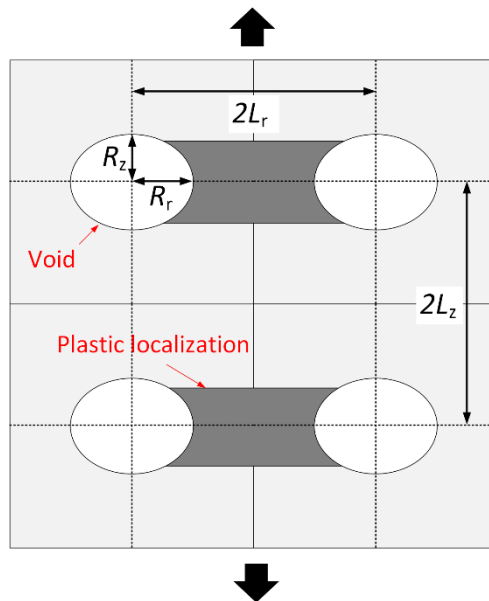
351

352   *Figure 10 The dimension parameters in the equation of I factor*

353   Ductile fracture is assumed to initiate when the onset of void coalescence criterion is satisfied over the

354   characteristic length l^*, the associated expression can be written as:

20

$$\frac{\sigma_{max}}{\sigma_0} - I(\chi) \geq 0 \quad for \quad r \geq l^* \tag{7}$$

The schematics of this approach is shown in Figure 11, the variations of σ_{max}/σ_0 and $I(\chi)$ in front of the crack tip at various J levels ($J_1 < J_2 < J_3$) are plotted. As the applied load increases, I factor decreases while σ_{max}/σ_0 remains relatively constant. The fracture initiation condition is satisfied over a gradually increasing distance until the distance exceeds the characteristic length l^* and then the initiation of ductile fracture criterion is reached.
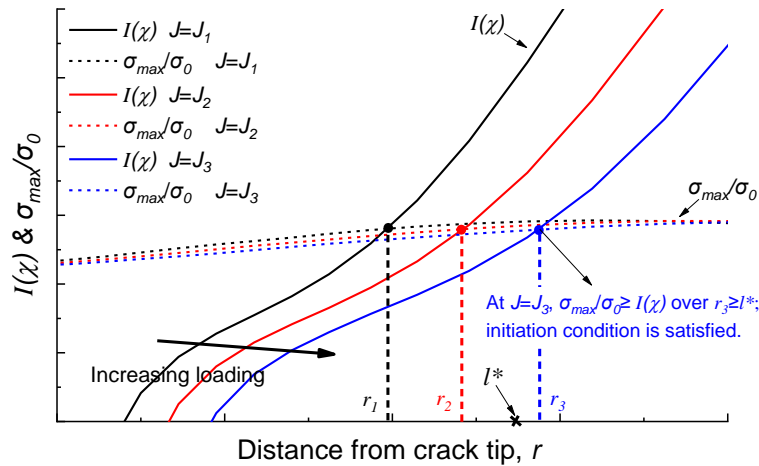
Figure 11 Schematic of the micromechanical approach in characterizing fracture initiation

5.2 Calibration of the parameters of the analytical method (χ_0 and l^*)

Two parameters in the micromechanical model require calibration: the characteristic length l^* and the initial relative void spacing χ_0. The critical parameters were determined from the testing and finite element analysis of both the notched round tensile specimen and miniature compact tension specimen. The tests were conducted to identify the critical load or $J_{0.2mm}$ corresponding to the fracture initiation. The finite element simulations were performed to investigate the local mechanical parameters at the critical initiation load or $J_{0.2mm}$ which was obtained from the testing [27], therefore building the connection between the overall fracture state and the local mechanical properties of the material.

The initial relative void spacing χ_0 is the first parameter to be calibrated. As shown in Figure 12(a), the initiation of the ductile fracture in the notched round tensile specimen is determined as the moment at which a sudden drop of the applied load occurs. In the notched tensile specimen, the ductile crack

374   initiation usually takes place in the center region of the narrowest cross section. In particular, the fracture

375   initiation is insensitive to the characteristic length l^* because of the relatively moderately uniform

376   distribution of the stress and strain at the fracture section. Therefore, the crack initiation in a notched

377   round tensile specimen is assumed to occur when the onset of void coalescence criterion is satisfied at the

378   center of the fracture section. As shown in Figure 12(b), for specimen N130, at the load corresponding to

379   the experimentally determined crack initiation, the onset of void coalescence criterion is achieved at the

380   center of the narrowest cross section ($\sigma_{max}/\sigma_0 \geq I(\chi)$) when $\chi_0 = 0.0456$, which is related to a reasonable

381   level of initial void volume fraction f_0=0.00006. Same calibration procedure is then repeated based on the

382   critical cross section radius (in Table 4) measured from six notched round tensile specimens. As shown in

383   Figure 12(c), smaller χ_0 values are derived from the specimens with smaller critical cross section radius,

384   which makes sense since later fracture indicates less initial void porosity, that is smaller χ_0. The obtained

385   χ_0 values are summarized in Figure 12(d), the average yields the value of 0.048, the 95% confidential

386   bound ranges from 0.032 to 0.064. Since the χ_0 value of 0.0456 determined above is well within the 95%

387   confidential bound and close to the average value, $\chi_0 = 0.0456$ is now assumed fixed throughout the
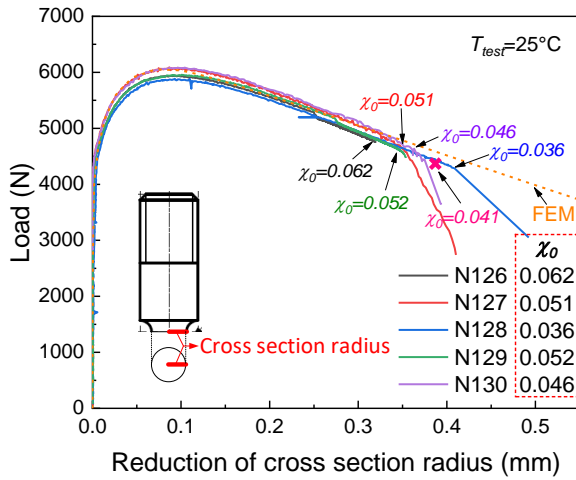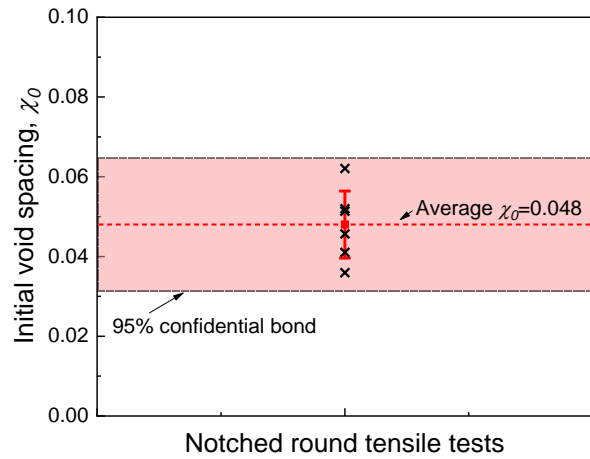
388   analysis in this paper.

389

390


(a)   (b)

(c)

(d)
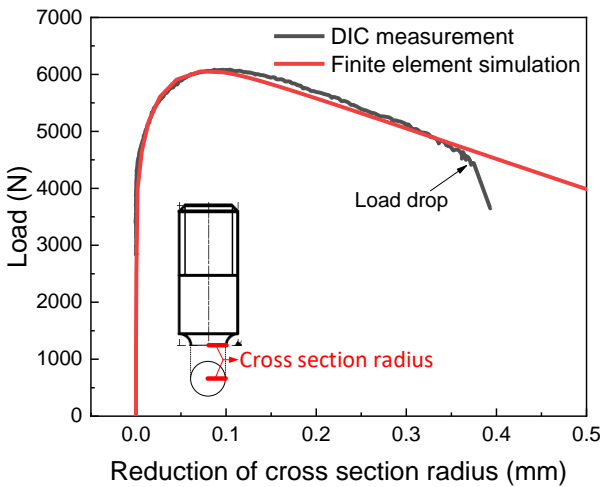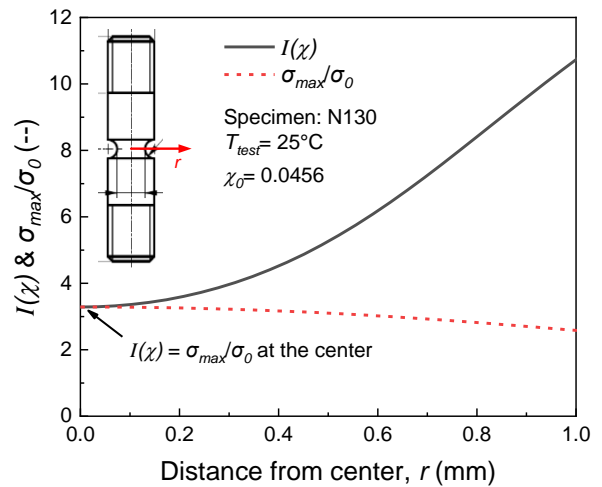
Figure 12 (a) Load versus cross section radius curves obtained from finite element analysis and DIC measurement (b) Radial distributions of σ_{max}/σ_0 and $I(\chi)$ on the narrowest cross section at fracture initiation of N130 (c) Experimental load versus cross section curves of six tests on notched round tensile specimens (d) Summary of the χ_0 determined from the six tests

The characteristic length scale $l*$ associated with the ductile fracture initiation [28] is needed to rationalize the data and load to a finite amount of energy spent in the fracture process zone as a result of the intrinsic spacing between voids. Mini-CT specimens with highly constrained pre-crack (a_0/W = 0.5) were tested to calibrate the characteristic length $l*$ in the micromechanical framework, at two temperatures (RT and 290°C) to provide different $J_{0.2mm}$ value and thus enlarge the calibration basis. Figure 13(a) provides the average and the uncertainty bounds of the $J_{0.2mm}$ generated from the test data in Table 4, the average value yields 203 kJ/m^2 at RT and 178 yields kJ/m^2 at 290°C, showing a strong dependence on the test temperature. In the calibration procedure addressed next, the characteristic length $l*$ is determined by using the $J_{0.2mm}$ measured from the tests with the data pairs of J-integral and trial characteristic length from the finite element simulations. As shown in Figure 13(b), for a given choice of trial length scale, the J-integral where the Thomason criterion is first satisfied (when $\sigma_{max}/\sigma_0 \geq I(\chi)$ for $0 \leq r \leq l*$) is calculated from the finite element simulation. The $J_{0.2mm}$ values measured from mini-CT tests are also plotted in the figure, then the $l*$ is determined as the value that matches the experimental $J_{0.2mm}$ value. Thus, for mini-CT specimens tested at room temperature, the $l*$ value is determined to be 0.232 mm ($l*/W$ = 0.028), similarly for the mini-CT specimens tested at 290 °C, the $l*$ value is 0.226 mm ($l*/W$ = 0.0272). The close

410   agreement between the calibration results at 25 °C and 290 °C demonstrates that l^* is almost constant for

411   one selected material independent on the test temperature.
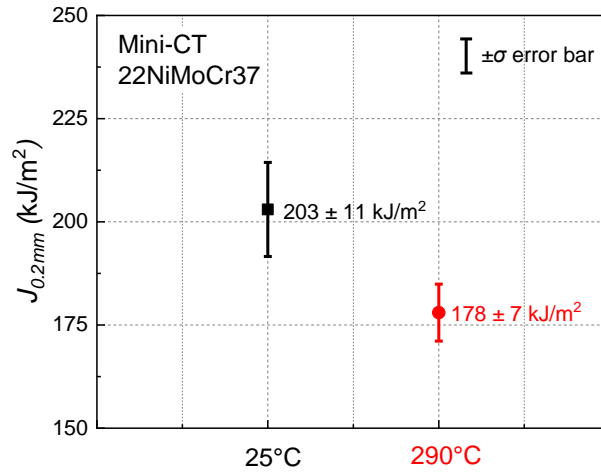
(a)
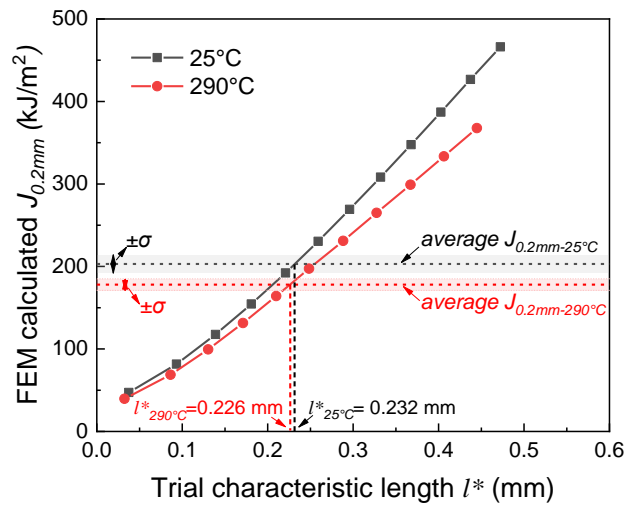
(b)

412   *Figure 13 (a) Summary of the $J_{0.2mm}$ of mini-CT geometry at 25 °C and 290 °C (b) Determination of l^* for 25 °C and 290*

413   *°C based on trial l^* and $J_{0.2mm}$*

414   To verify that the calibrated characteristic length is within a reasonable range, more physical explanations

415   of the characteristic length are required by examining the microstructure of the tested specimens.

416   Hancock and Mackenzie noted that the physical event leading to the ductile fracture is primarily the

417   connection (through the formation of the shear bands) of two or more large holes formed from coalescing

418   inclusion colonies [29, 30]. Among them, the distance between two large holes represents the minimum

419   amount of material that may trigger a ductile fracture. In order to capture the microstructure at fracture

420   initiation, three notched round tensile bars (N126, N129 and N131) were tested at room temperature and

421   interrupted at a minimum load increment after the load drop (as shown in Figure 14). After the tests, the

422   specimens were cut longitudinally, then polished, and finally examined under a 3D microscopy. As shown

423   in Figure 15, the approximate range of the characteristic length was determined by measuring the

424   distances between the holes that were already linked together and the holes that were potentially linked

425   together. Each specimen was polished two to three times to obtain sufficient enough samples, leading to

426   a total of 170 measurements. Since the characteristic length in this paper was characterized by the defects

427   formed from the inclusions originally in the material, the measured distances between the holes need to

428   be corrected to their corresponding equivalent value before deformation. As shown in Figure 16(a), the

429   correction was conducted based on the finite element model that was loaded up to the same deformation

430   level, the original spacing between the inclusions was obtained by measuring the original distance of the

431   nodes in the finite element model that has the same deformed position with the holes observed in the

432   microscope. The distances after the correction are plotted in Figure 16(b), the measurements on seven

433   polished surfaces show close average values, the result of all the measurements yields the value of

434   174.2 ± 99 μm, which incorporates well the previously calibrated characteristic length.
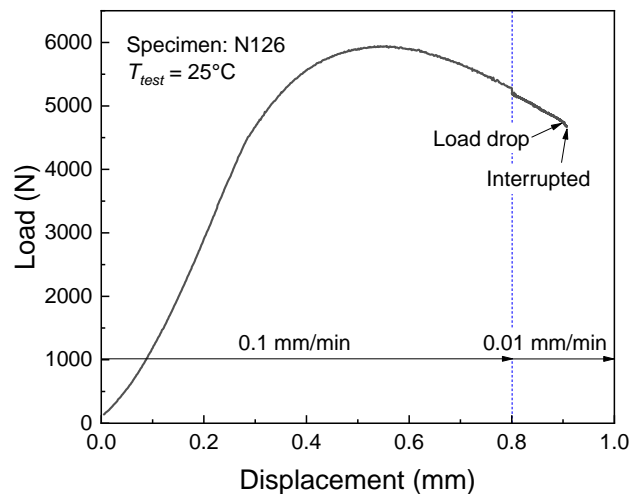
435

436   *Figure 14 Experimental load versus displacement curve of the interrupted tensile test on specimen N126*
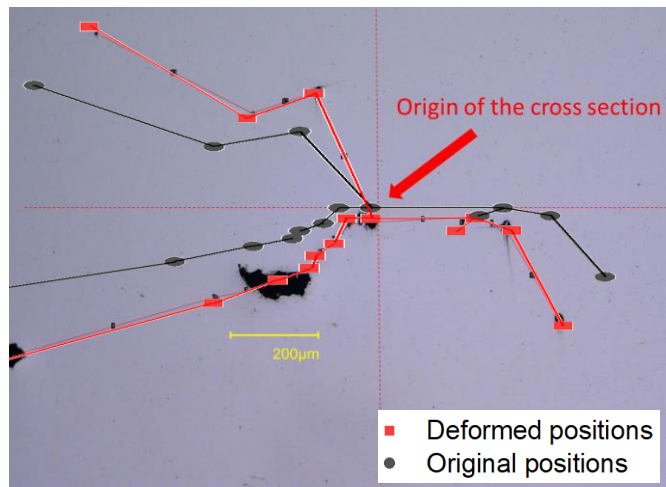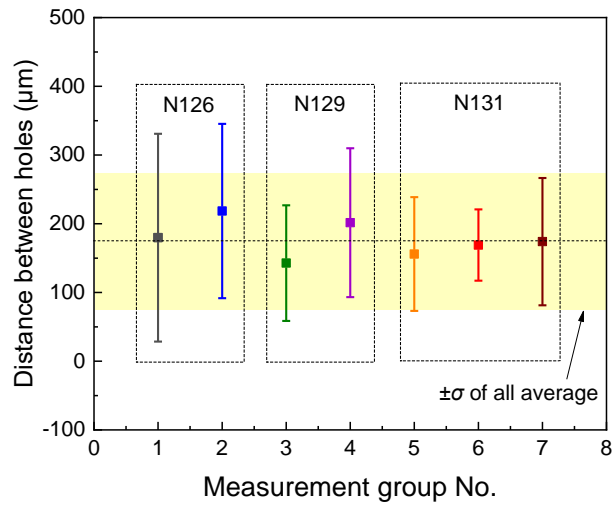
437
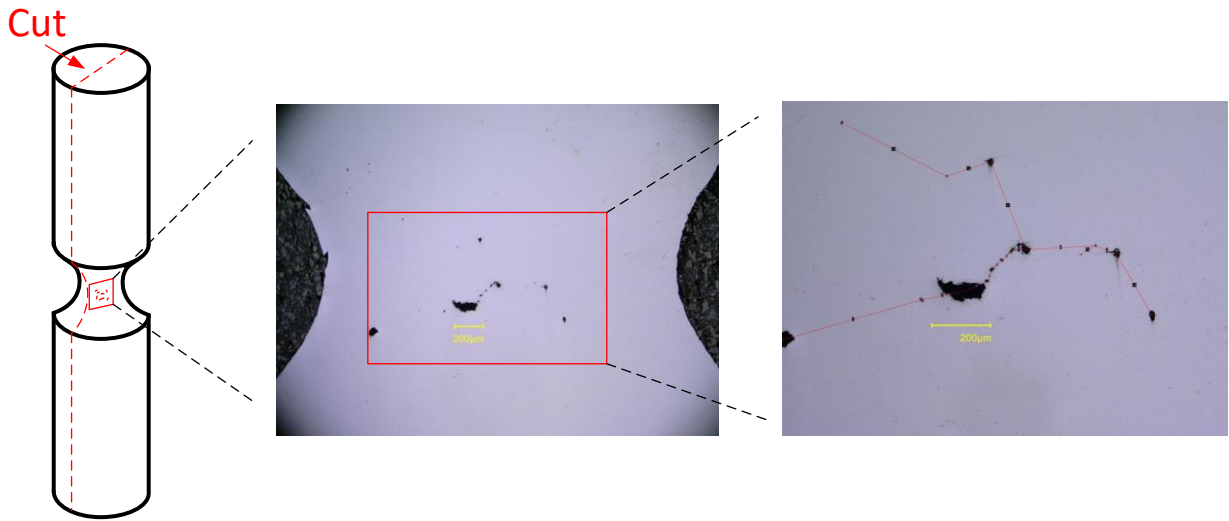
Figure 15 The measurement of the distance between the holes on the longitudinal section of a notched round tensile specimen using 3D microscopy

438

439

440

(a)

(b)

Figure 16 (a) The correction of the measured distances between the holes (b) Summary of the measured distances after correction

Another approach [30] suggests measuring the length of the dimple valleys that can be observed on the fracture surface using an SEM (see Figure 17). The formation of the valleys has the same physical mechanism as the physical event that is mentioned above, the valleys are indicative of the linked holes or inclusion colonies after test, representing therefore the minimum volume of material required to initiate fracture. An average length of 155 ± 67 µm was determined based on the measurements of 107 valleys on the fracture surface of five fractured mini-CT specimens, the results are displayed in Figure 18. It is worth noting that, as crack propagation is not considered in the present FEM model, it is somewhat difficult to provide accurate correction of the measured valley size to the state before deformation. Therefore the measured range of l^* is underestimated, nevertheless, the previously defined values of l^* are only slightly above the upper bound of the measurements. Moreover, the calibrated characteristic length is comparable to the length scale determined previously for structural steels. Hill and Panontin proposed a characteristic length of 0.15 mm for 7050 aluminum [31]. Chi and Kanvinde determined the characteristic length of seven steels with the strengths ranging from 330 MPa to 800 MPa, yielding the value from 0.13 mm to 0.3 mm [32]. Additional study conducted by Kanvinde et al. also provided close characteristic length values of 0.2 mm, 0.11 mm and 0.08 mm for mild A572 Grade 50 steel and two types of Grade 480 MPa weld filler materials, respectively [33, 34]. Thus, in the analysis to be discussed, a fixed value of the characteristic length $l^* = 0.23$ mm is adopted, which is the average value of the $l*$ calibrated at RT and 290°C.
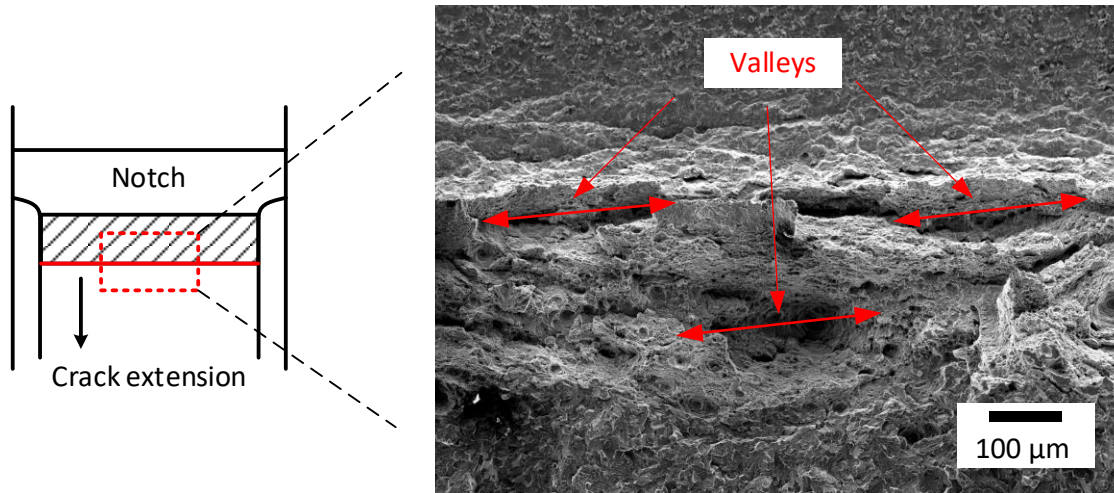
Figure 17 The measurement of the valleys on the fracture surface of a mini-CT specimen using SEM
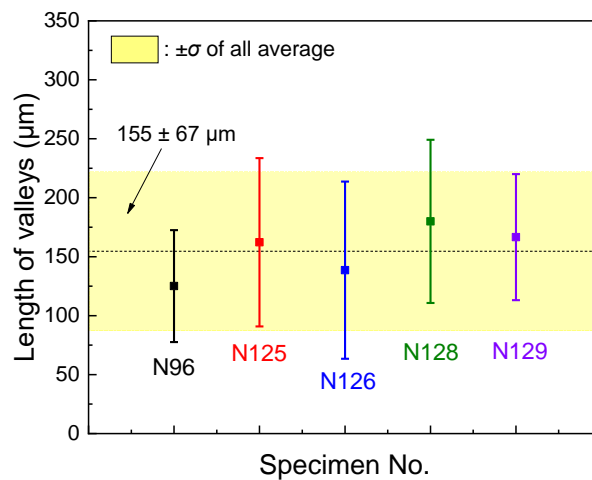

Figure 18 Summary of the measured length of the valleys

5.3 Comparison of the initiation load and initiation position for various pre-crack fronts

This section describes the application of the calibrated micromechanical-based approach for ductile fracture initiation based on the finite element simulations. Here, we investigate the mini-CTs ($a_0/W = 0.5$) with uniform and tilted initial cracks using the material properties at room temperature. As discussed in the previous sections, the inclination of the initial crack front redistributes the stress triaxiality and the equivalent plastic strain on the ligament of the specimen, thus affecting the crack initiation at different thickness positions. Figure 19(a) and Figure 19(b) provide the difference between σ_{max}/σ_0 and $I(\chi)$ (Eq.4) at different thickness positions in front of the uniform and tilted pre-crack, the load level corresponds to

473 the experimentally measured $J_{0.2mm}$ at RT. In the plots shown in Figure 19(a), the curve of the mid-thickness

474 position has the largest distance range above 0, followed by the thickness position next to it. In particular,

475 only the distance range ($\sigma_{max}/\sigma_0 - I(\chi) > 0$) at the mid-thickness position covers the l^*, indicating the earliest

476 fracture initiation. This analysis provides reliable estimates recalling the experimental observations. Figure

477 19(b) gives the distribution of the difference value ($\sigma_{max}/\sigma_0 - I(\chi)$) at various thickness positions ahead of

478 the tilted initial crack, the calibrated l^* is also plotted for reference. At the J level corresponding to the

479 experimentally measured $J_{0.2mm}$ on the mini-CT geometry with a valid pre-crack front at room temperature,

480 none of the thickness positions meet the initiation condition of the ductile fracture ($\sigma_{max}/\sigma_0 - I(\chi) \geq 0$ for r

481 $\geq l^*$), which suggests that this pre-crack configuration tends to have an even larger critical fracture

482 toughness. Among them, the thickness positions $x/B_N = 1/2$ and $x/B_N = 5/8$ have similar larger length scale

483 with $\sigma_{max}/\sigma_0 - I(\chi) > 0$, indicating the most likely positions for the fracture initiation. The thickness positions

484 $x/B_N = 3/8$, 3/4 and 7/8 have relatively weaker chance of triggering the ductile fracture first. Thus, the

485 following determinations of the $J_{0.2mm}$ value of the mini-CTs with different pre-cracks are based on the

486 thickness positions with higher potential to trigger ductile fracture that were addressed above.

487 Figure 19(c) provides the variation of FEM-calculated $J_{0.2mm}$ with different trial characteristic length at the

488 mid-thickness position of uniform pre-crack, at the $x/B_N = 1/2$, $x/B_N = 9/16$ and $x/B_N = 5/8$ of tilted pre-crack.

489 The results at the thickness position $x/B_N = 3/8$ are also provided to show the effect of pre-crack non-

490 uniformity on the two positions that are symmetrical along the mid plane. The vertical dashed line

491 represents the calibrated l^*, thereby the $J_{0.2mm}$ value is determined as the J corresponding to the

492 intersection point of the curves with this dashed line. Clearly, for the tilted pre-crack configuration, the

493 initiation of ductile fracture at the mid-thickness position is satisfied at the lowest J value over the

494 characteristic length scale, followed by the thickness positions $x/B_N = 9/16$, $x/B_N = 5/8$ and then the

495 thickness position $x/B_N = 3/8$. Therefore, for the mini-CT specimen with sharp fatigue pre-crack, FEM

496 simulation results show that the initiation position of the ductile fracture is located rather close to the

497 mid-thickness position. Further, it is observed that the $J_{0.2mm}$ value of the mini-CT with uniform pre-crack

498 yields a value of 201 kJ/m^2, the $J_{0.2mm}$ value of the mini-CT with tilted pre-crack yields $J_{0.2mm}$ = 210 kJ/m^2.

499 Therefore the pre-crack non-uniformity increases the FEM-calculated $J_{0.2mm}$ by 9 kJ/m^2, providing the fact

500 that similar global J-integral is extracted from the two pre-crack configurations, the tilted pre-crack

501 configuration has a negligible effect on the ductile crack initiation. The similar slopes of the curves in the

502 figure mean that the above conclusion is still valid even when another l^* in the range 0.226 mm $\leq l^* \leq$

503 0.232 mm is adopted.

(a)

(b)

(c)
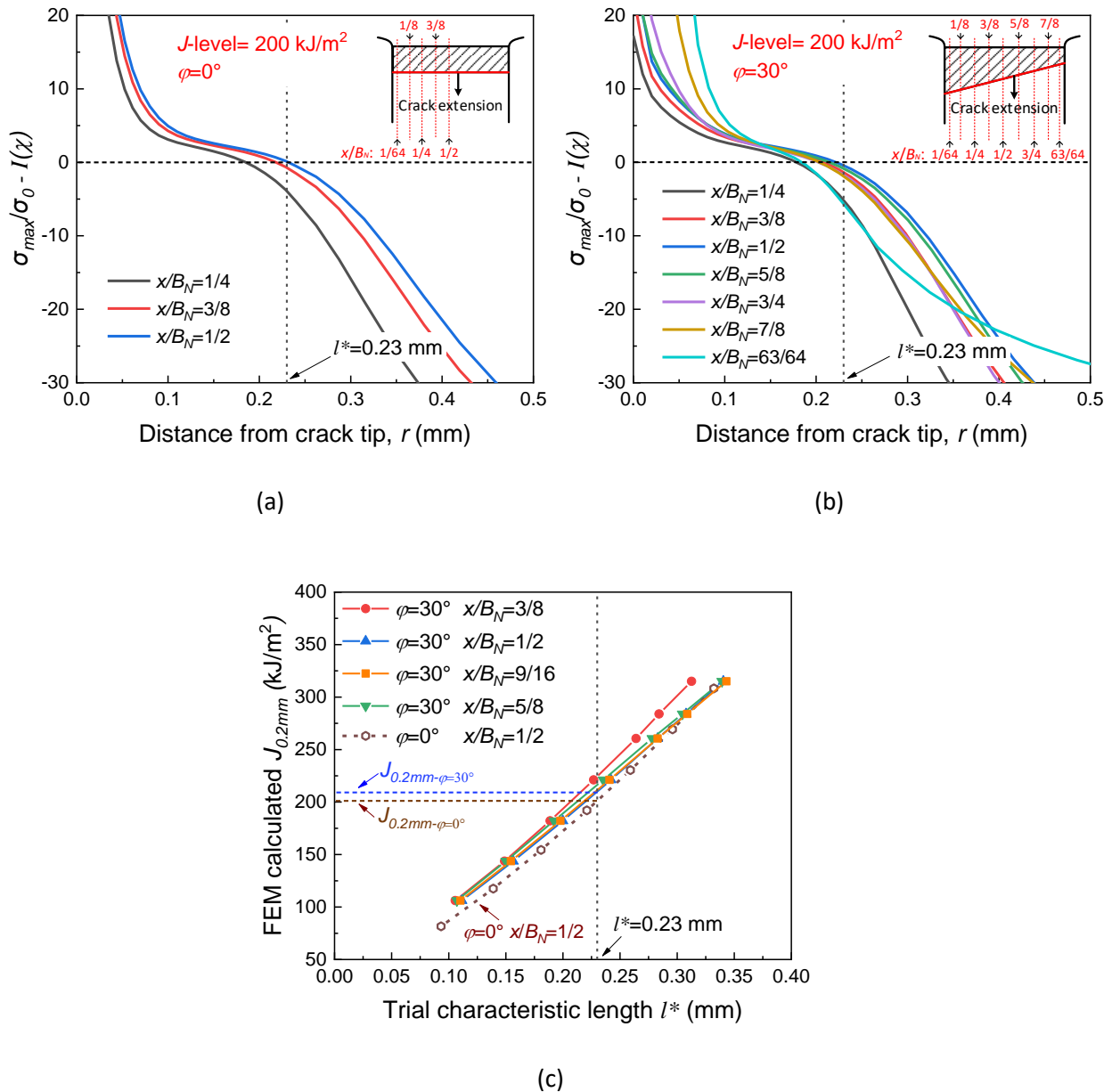
Figure 19 *The distribution of difference value between σ_{max}/σ_0 and $I(\chi)$ on the ligament in front of (a) uniform pre-crack front and (b) tilted pre-crack front. (c) Determination of $J_{0.2mm}$ for uniform and tilted pre-crack configurations*

The above discussion clearly reveals the negligible effect of pre-crack non-uniformity on the initiation of ductile fracture for the fatigue pre-cracked mini-CT samples. Additional analysis of the effect of crack front notch radius on the simulation results is carried out to provide evidence for the subsequent experimental verifications using the mini-CT specimens containing EDM (electrical discharge machining) notch. Figure 20 plots the estimates of the $J_{0.2mm}$ with a series of trial characteristic lengths, the final determined $J_{0.2mm}$

is the $J_{0.2mm}$ corresponding to the calibrated $l*$ as outlined above. It is shown that for the mini-CT with tilted EDM notch (notch radius = 50 μm), half of the crack front near the shallow crack side has a higher probability of triggering ductile fracture. The difference of the results at the thickness position $x/B_N = 1/2$, $x/B_N = 9/16$ and $x/B_N = 5/8$ is rather small, in particular, the fracture initiation condition is satisfied at the lowest J at the thickness position $x/B_N = 9/16$. Therefore, it can be reasonably demonstrated that the initiation position is located at the portion of crack front between the mid-plane and the $x/B_N = 5/8$ thickness position. Further, comparing the determined $J_{0.2mm}$ of mini-CT with uniform and tilted EDM notch based on the various thickness positions, the FEM calculations yields the $J_{0.2mm}$ value for the mini-CT with uniform and tilted EDM notch as 223 kJ/m² and 239 kJ/m², respectively. The computed $J_{0.2mm}$ values are higher than that for the model of the fatigue pre-crack configuration due to larger crack tip notch radius. Recalling the difference of 9 kJ/m² determined from sharp fatigue pre-crack configurations, the difference between $J_{0.2mm-EDM-0°}$ and $J_{0.2mm-EDM-30°}$ is still remarkably small. This is suggesting that the crack front inclination has a rather limited effect on the $J_{0.2mm}$ values that are obtained from the mini-CTs with different initial EDM notches. However, it is also possible that the difference between the $J_{0.2mm-0°}$ and $J_{0.2mm-30°}$ measured from the experiments is larger because of test uncertainties.
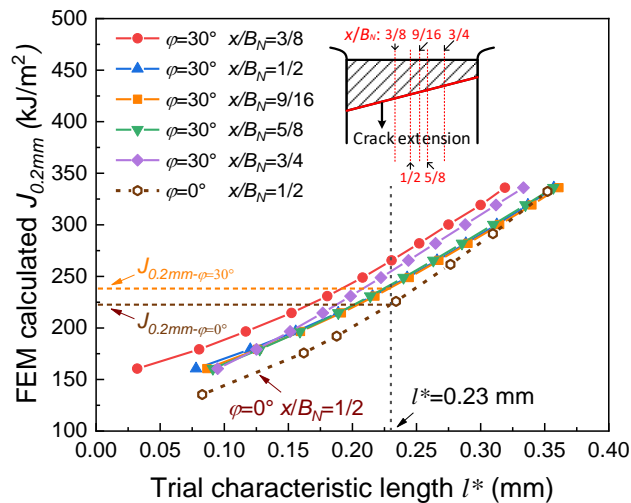
Figure 20 Determination of $J_{0.2mm}$ for the mini-CT specimens with uniform and tilted initial EDM notch

5.4 Experimental verification of the simulation results

Eighteen fracture toughness tests were performed to provide experimental observations of the effect of crack non-uniformity and to verify the observations in the finite element analysis and the simulation results using the micromechanical based model. A typical RPV steel, 22NiMoCr37, was investigated, all the

specimens were 20% side grooved and were tested at RT. In order to obtain the ideal initial cracks as that in the finite element analysis, the uniform initial crack and tilted initial crack were machined using the electrical discharge machining technology (EDM). For each specimen configuration, the mini-CT specimens were loaded up to different CMOD levels, the details of each test are shown in Table 5.

Table 5 List of the fracture toughness test parameters and results

| Temperature (℃)	Initial crack type	Specimen No.	CMOD level (mm)	Δa (mm)	J_{end} (kJ/m^2)
25	Uniform	N106	0.56	0.148	149.2
		N98	1.10	0.286	294.1
		N124	1.00	0.278	293.8
		N126	1.50	0.542	397.5
		N125	1.65	0.639	453.4
		N96	1.93	0.915	515.3
		N104	2.20	1.174	564.2
		N100	2.80	1.681	668.1
		N102	3.67	2.321	601.8
	30° tilted	N105	0.55	0.132	145.8
		N103	0.90	0.308	241.9
		N127	1.00	0.330	293.2
		N129	1.50	0.625	405.0
		N128	1.65	0.683	435.6
		N109	1.87	0.846	509.4
		N97	2.20	1.224	550.9
		N101	2.80	1.632	667.1
		N107	3.67	2.319	611.1

Δa: measured final crack extension (including blunting area); J_{end}: average J-value at the end of the test using three techniques (max. CMOD level)

During testing, three techniques, i.e., the unloading compliance (UC), the normalization data reduction (NDR) and the energy normalization (EN) were used for the analysis of the crack extension of each test. After testing, the specimens were heat tinted and then broken in liquid nitrogen to better identify the ductile crack propagation area. 3D digital microscopy measurements were then performed based on the

542   9-point method to provide accurate final crack extension data (as listed in Table 5). Additionally, for the
543   specimens with small amount of ductile tearing (N106, N98, N124, N105, N103 and N127), in order to
544   correctly capture the extension area, the measurements were carried out on the SEM photos of the
545   fracture surface. The final crack extension Δa plays a key role in the comparison of different initial crack
546   configurations, which, further being used in this study in the generation of the J-R curves (based on
547   multiple specimen method) and in the investigations on the initiation of ductile fracture.

548   Figure 21 shows the experimental load-CMOD curves obtained from six (3 for each crack configuration) of
549   the fracture toughness tests. Before the initiation of ductile fracture, these curves are in close agreement
550   with one another. This feature indicates a negligible effect of initial crack non-uniformity on applied load,
551   which is consistent with the observations that were found in the finite element analysis. It is worth noting
552   that, after the crack starts to propagate, the tilted initial crack configuration tends to have a lower applied
553   load than that for the uniform initial crack configuration. This can be illustrated by investigating the
554   characteristics of crack propagation of the uniform initial crack and the tilted initial crack. The fracture
555   surfaces of the two initial crack configurations at three CMOD levels: 0.55 mm, 1 mm and 1.9 mm are
556   shown in Figure 22. Significant difference in the way of propagation is observed. For the mini-CT specimen
557   with uniform initial crack, the crack grows equally across the specimen thickness. On the other hand, for
558   the tilted initial crack, the amount of crack propagation near the side with shallower crack is significantly
559   larger than that on the other side due to the higher potential of cracking. As a result, in the case of tilted
560   initial crack, the crack front is rotating with the increasing applied load until it is perpendicular to the two
561   free boundaries. The process of the rotating of crack front is the result of the combined action of the
562   opening mode fracture and the tearing mode fracture. The anti-plane shearing in the tearing mode
563   fracture reduces the load that is applied perpendicular to the fracture surface, resulting in a reduction of
564   the load-CMOD curve particularly in the range after the crack starts to propagate. Figure 23 shows the J-R
565   curves obtained from the tests on the specimen N96 (mini-CT with uniform initial crack) and N109 (mini-
566   CT with 30° tilted initial crack) using the NDR and EN techniques. It can be observed that the J-integral
567   values of the two initial crack configurations are in close agreement. This provides evidence of the limited
568   effect of the crack front non-uniformity on the global J-integral. Further details of the effect of crack front
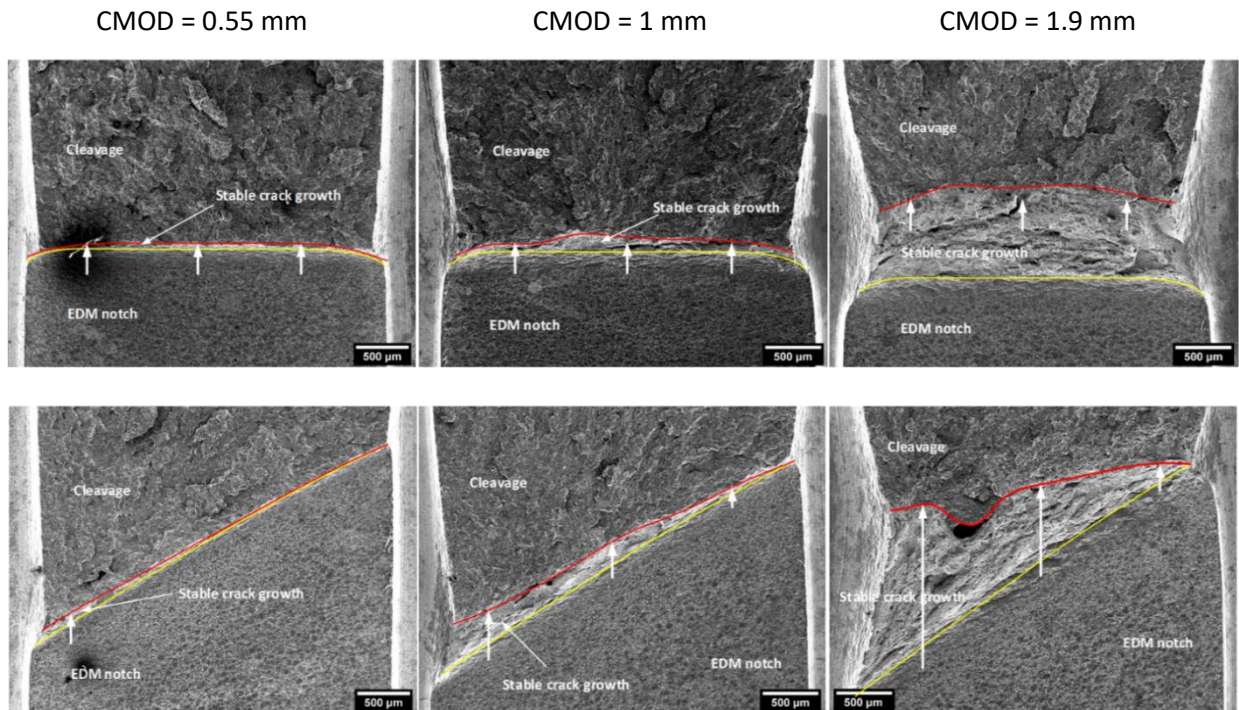569   configuration will be addressed later in section 5.4.2.
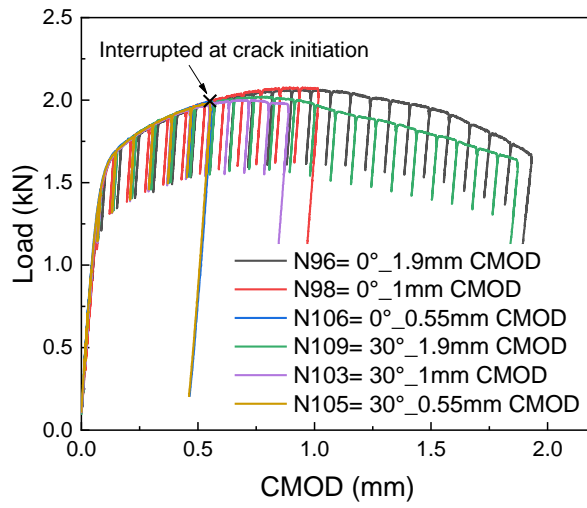
Figure 21 Load versus CMOD curves obtained from fracture toughness tests

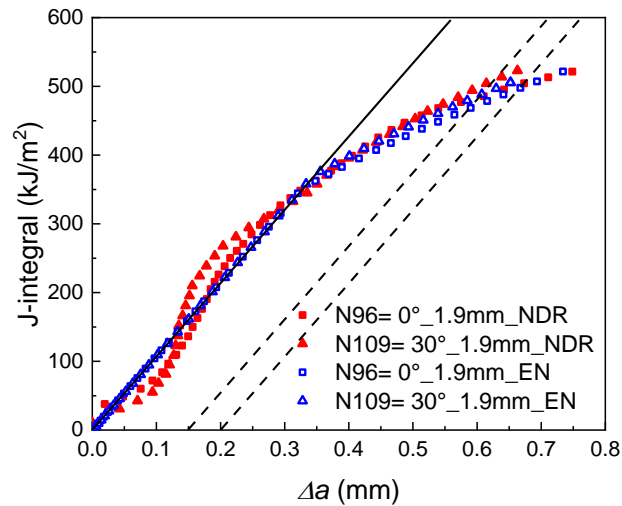CMOD = 0.55 mm   CMOD = 1 mm   CMOD = 1.9 mm

Figure 22 The fracture surface of the propagated uniform initial crack and the tilted initial crack at three CMOD levels

Figure 23 J-R curves obtained from the specimen N96 and N109 using NDR and EN techniques

577 ## 5.4.1 Analysis of the microscopic fracture mechanism

578

579 Figure 24(a) displays the scanning electron microscopy (SEM) images of the fracture surface of specimen

580 N96. It is a mini-CT specimen with a uniform fatigue pre-crack, which shows clear characteristics of ductile

581 fracture. Four regions (A, B, C and D) close to the initial crack front located at three thickness positions

582 from the center to the free boundary clearly reveal different features. The large and equiaxed dimples are

583 mainly distributed in region A (center x/B_N = 1/2) and region B (x/B_N = 1/4). Close to the free surface, in

584 region C (x/B_N = 1/64), the shear band (the stretching direction is indicated by blue arrows) can be observed

585 where smaller and elongated dimples exist. This is exhibiting a transition from tension dominant fracture

586 in the center to shear-slip dominant fracture when it is closer to the free boundary. Notably, the

587 microstructure characteristics in the SEM images correspond to the numerically predicted $I(\chi)$

588 distribution at different thickness positions ahead of various EDM notches shown in *Figure 25*(a). As

589 addressed in the previous section, $I(\chi)$ indicates the critical load leading to void coalescence, a lower $I(\chi)$

590 indicates a lower load limit and thus a more fully developed microstructure towards ductile fracture. It is

591 clear that the $I(\chi)$ level decreases from the free boundary to the center. Smaller $I(\chi)$ accelerates the void

592 growth and coalescence, leading to the formation of large dimples in the center region. The transition of

593 fracture behavior from center to both sides discussed above also highlights the shift of $I(\chi)$ level.

594 Moreover, the opening of the small dimples along the shear lip and the stretch direction of the shear bands

595   (blue arrows) exhibit that the local fracture in region D (close to the free surface) is directed to the inner

596   part of the specimen.

597   Similarly, Figure 24(b) shows the SEM images of the fracture surface of specimen N109 with a 30° tilted

598   initial crack. Different fracture characteristics can be seen from larger magnification images (A, B, C, D and

599   E) at five positions from one free boundary to another. Region B (x/B_N = 3/4), C (x/B_N = 1/2) and D (x/B_N =

600   1/4) are located near the center area. It can be clearly observed that the fracture surfaces in these regions

601   have the appearance of a rough fracture surface with large and deep dimples. As compared to the center

602   region B, C and D, only shallow dimples and enlarged voids exist in region A (shallow initial crack, x/B_N =

603   63/64) and region E (deep initial crack, x/B_N = 1/64). Especially for the region close to the free boundary,

604   an increased dominance of shearing effect is observed. The difference of the fracture behavior exhibited

605   by the SEM images can be explained in terms of the FEM results shown in Figure 9(c), Figure 9(e) and *Figure*

606   *25*(b). The crack propagation from the center region to the side with shallow initial crack (region A, B, C

607   and D) is fully developed due to lower $I(\chi)$ level. Nevertheless, the dominance of either the stress

608   triaxiality or the equivalent plastic strain leads directly to the differing fracture process zone

609   characterizations at the center region (region B, C and D) and the region close to the free boundary (region

610   A). The highly concentrated stress triaxiality level near the center region (x/B_N = 1/4, 1/2 and 3/4) increases

611   the amount of deep dimples in region B, C and D, the large equivalent plastic strain close to the shallow

612   initial crack (x/B_N = 63/64) leads to a large amount of shear bands in region A. It is further observed that

613   the portion of crack front in region E (deep initial crack, x/B_N = 1/64) is less involved in the damage process,

614   minor shear and propagation is found in this region because of remarkably high $I(\chi)$ level. Besides,

615   compared to the region B (x/B_N = 1/4) ahead of the uniform initial crack (in Figure 24-a), the region B (x/B_N

616   = 3/4) and D (x/B_N = 1/4) ahead of the tilted initial crack (in Figure 24-b) have smoother fracture surfaces,

617   the voids and dimples have the appearance of being affected by out-of-plane shear, which is due to the

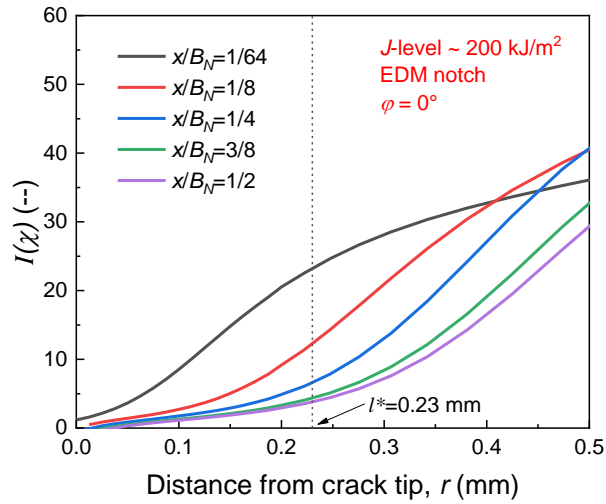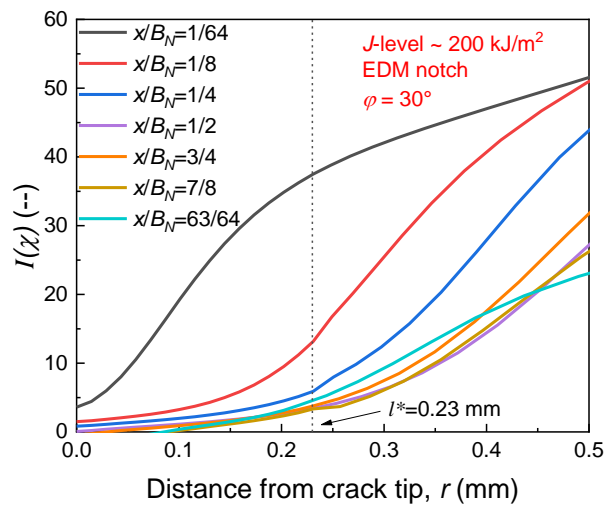618   combined influence of mode I and mode III loading.

619

620

(a)

621

(b)
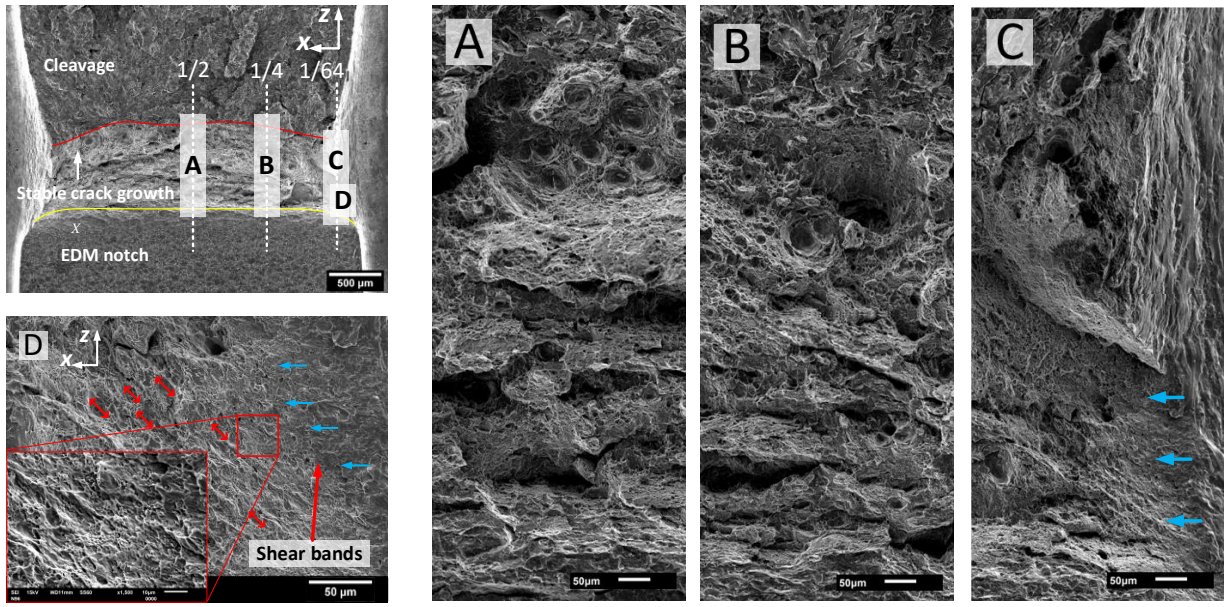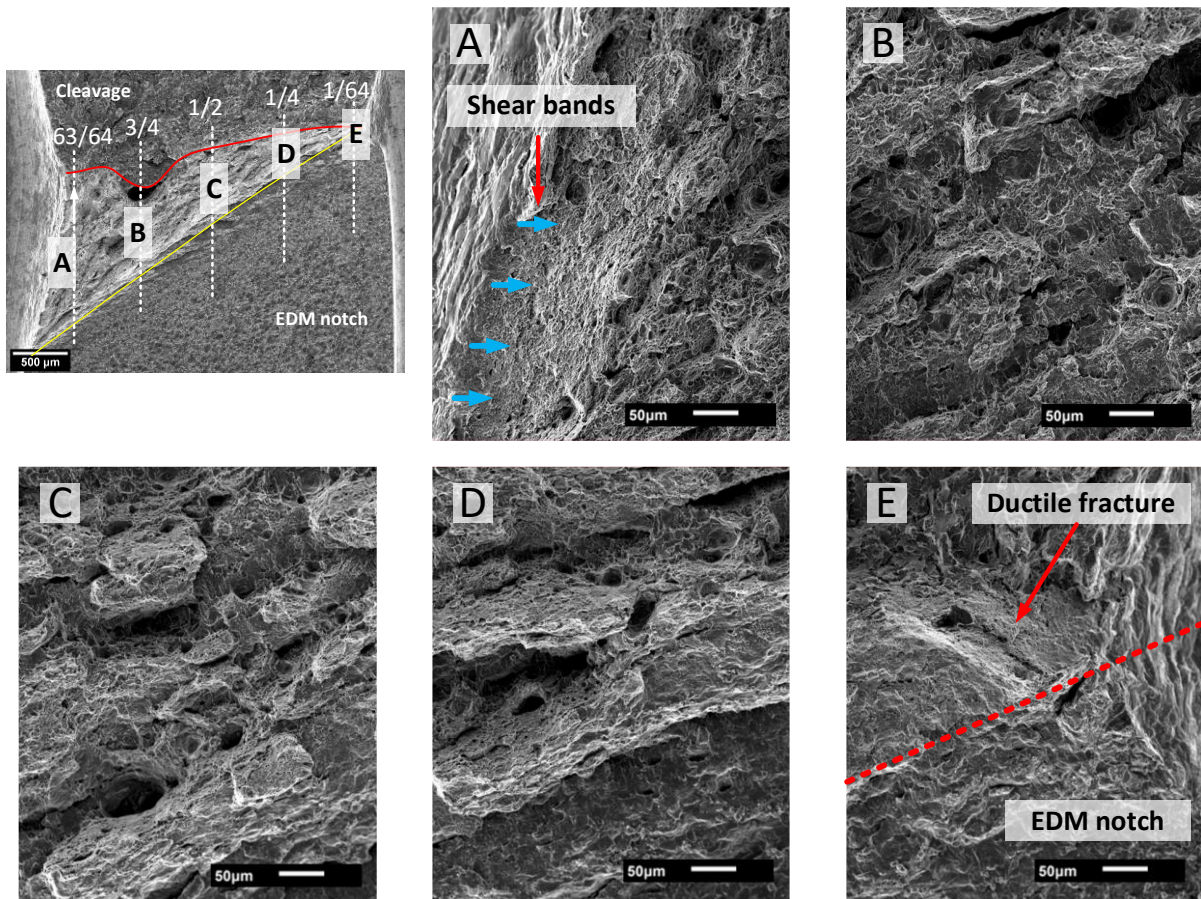
Figure 24 SEM images of the fracture surface at different positions (a) on the uniform initial crack front (N96, CMOD level ~ 1.9 mm) (b) on the tilted initial crack front (N109, CMOD level ~ 1.9 mm)

(a)

(b)

624   *Figure 25 The distribution of I(χ) on the ligament in front of (a) uniform initial EDM notch (b) tilted initial EDM notch*

625   Additional evidence is provided by examining the unloading compliance at the beginning of the test N96

626   and N109. *Figure 26*(a) displays the experimental load-CMOD curve in the elastic stage. As it can be seen

627   from the figure, at three CMOD levels, the unloading compliance of the mini-CT with tilted initial crack is

628   slightly smaller than that for the mini-CT with uniform initial crack. We can argue that at the beginning of

629   loading, an earlier crack tip blunting is found on tilted initial crack front. The loading behavior displayed in

630   *Figure 26*(a) has a direct bearing on the distribution of equivalent plastic strain described in Figure 9(e). Due

631   to the geometry of the tilted initial crack, the portion of crack front with shallow crack receives a larger

632   load than that on the uniform initial crack (see *Figure 26*-b). Clearly, a larger applied load accelerates the

633 concentration of considerable equivalent plastic strain at the thickness position x/B_N = 63/64 as addressed
634 in Figure 9(e), leading thus to the early blunting for the tilted initial crack that is found in the experiment.
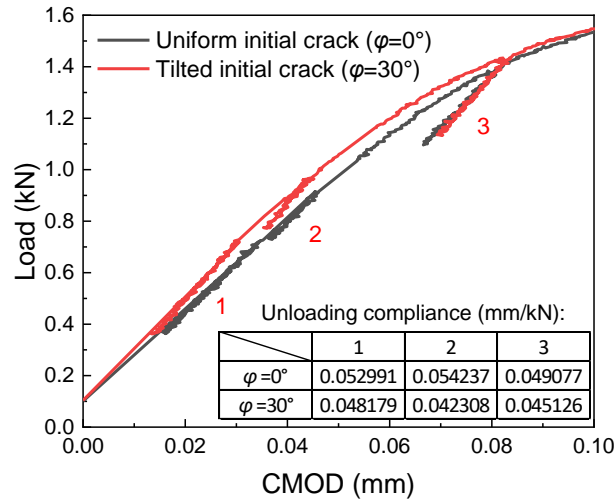
(a)
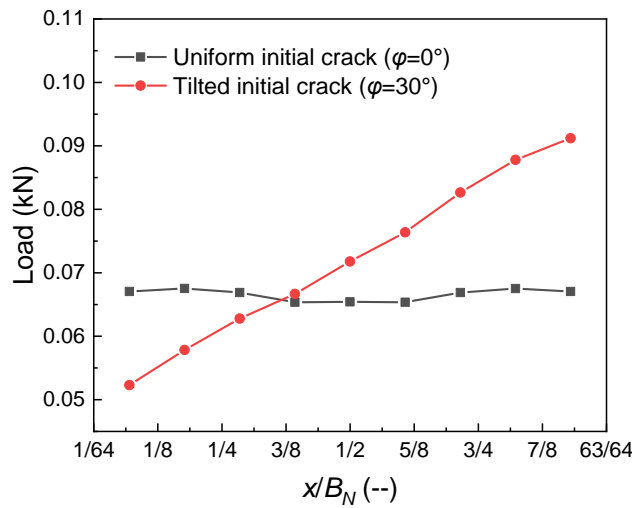
(b)

635 Figure 26 (a) Unloading compliance in the elastic region of the test N96 and N109 (b) Numerically predicted applied load
*636 across the thickness of specimen*

5.4.2 Microscopic observations with respect to the ductile fracture initiation

638 Based on the observations of the fracture behavior of specimens that were loaded up to CMOD equal to
639 1 mm and 1.9 mm, two mini-CT specimens N105 and N106 were loaded up to around 0.55 mm CMOD in

640   order to capture the onset of ductile fracture initiation. Figure 27(a) and Figure 27(b) show the SEM images

641   of the regions along the uniform crack front (N106) and the tilted crack front (N105), respectively.

642   Consider first the mini-CT specimen with uniform initial crack front, under the load level of CMOD = 0.56

643   mm, the ductile fracture occurs over the entire crack front. The larger crack propagation length in region

644   B and region C indicates that the fracture near the center area of the uniform crack front tends to initiate

645   first. For comparison, the initiation of the tilted initial crack is investigated by examining the same four

646   thickness positions on the crack front. It can be observed that for the same amount of CMOD, only a small

647   amount of ductile crack propagation is seen in region A (free boundary at the shallow crack) and B (center

648   region close to the shallow crack), whereas in region C (center region close to the deep crack) and D (free

649   boundary at the deep crack), there is no apparent measurable amount of stable crack growth, only the

650   pre-crack caused by EDM cutting and the blunting zone exist. Clearly, it indicates that ductile fracture is

651   more likely to initiate from the portion of the region between the mid-plane and the side with shallowest

652   initial crack, which agrees well with the micromechanical-based results of the crack initiation position given

653   in section 5.3. Moreover, under the applied load corresponding to CMOD = 0.56 mm, the measured crack

654   growth (excluding the blunting area) of the mini-CT with uniform initial crack is Δa = 25 µm, whereas Δa =

655   18 µm for the tilted initial crack configuration at CMOD = 0.55 mm. Apparently, the measurements show

656   rather small difference of the crack extension in front of two initial crack configurations for a given CMOD

657   level, indicating the critical initiation load in the real material displays limited dependence on the crack

658   front non-uniformity. Additional comparisons between the experimentally determined $J_{0.2mm}$ and

659   numerically computed $J_{0.2mm}$ were made and addressed in the following paragraph to support the adoption

660   of the micromechanical-based model and further discuss the effect of crack non-uniformity on the

661   engineering toughness behavior.

662

663

664   (a)

665

666   (b)
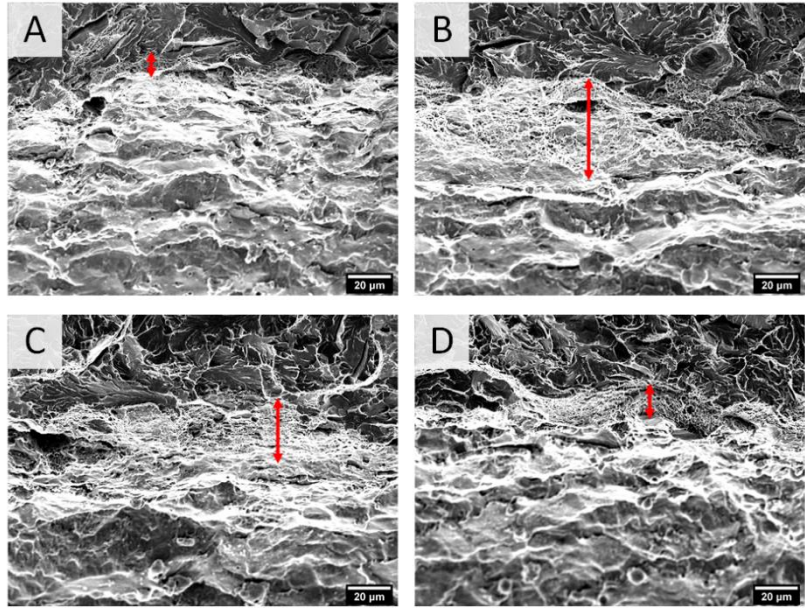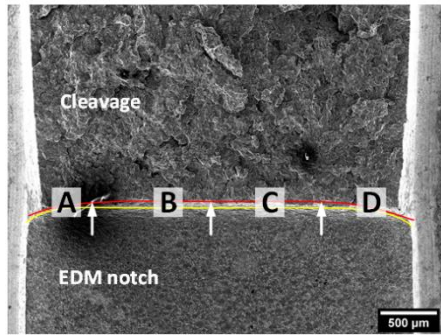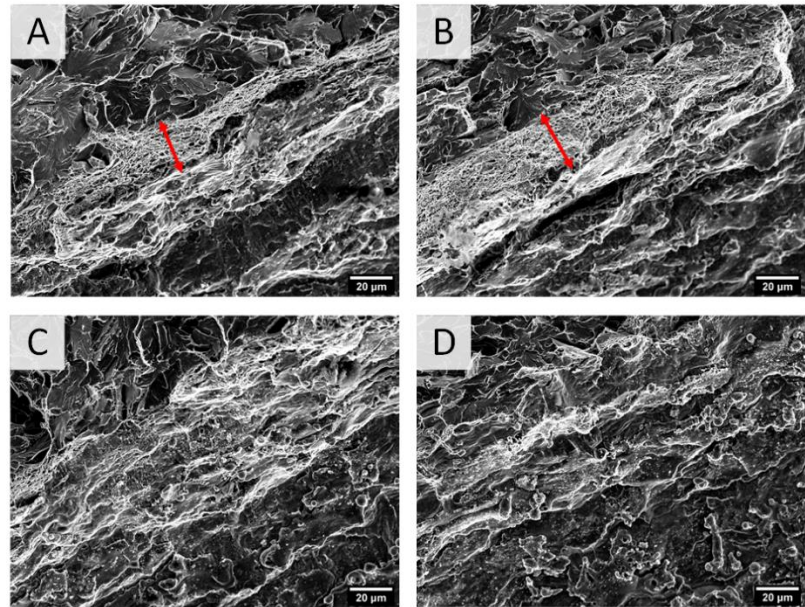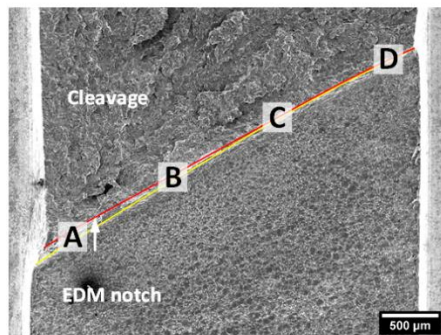
Figure 27 The SEM images of the fracture surface at different positions (a) on the uniform initial crack front (N106) (b) on the tilted initial crack front (N105) at a CMOD corresponding to the crack initiation

Figure 28 shows the J-R curves of the mini-CT geometries with uniform initial crack and 30° tilted initial crack generated using the multiple specimen method based on the test results in Table 5. The Δa - J_{end} data points obtained from the experiments are also plotted. Two mini-CT specimens with extremely large final crack extension, N102 (Δa = 2.321 mm) and N107 (Δa = 2.319 mm), are excluded from the determination

673   of J-R curves because the very small remaining ligament size is not sufficient to provide meaningful fracture

674   toughness results. It is found that the J-R curves exhibit close agreements with one another. The critical

675   toughness value ($J_{0.2mm}$) determined from the J-R curves and the $J_{0.2mm}$ computed based on the

676   micromechanical model and FEM simulations are listed in Table 6. Consider first the difference of the $J_{0.2mm}$

677   values between the two initial crack configurations. It is observed from the experimental results (EXP

678   column) that the initial crack inclination decreases the $J_{0.2mm}$ by about 25 kJ/m^2, showing a negligible effect.

679   A similar feature is expected for the numerical results (FEM column), the difference of $J_{0.2mm}$ is around 16

680   kJ/m^2. Although the $J_{0.2mm}$ for tilted crack configuration displays higher value numerically and displays

681   lower value experimentally, the small amount of deviation still represents a limited effect of crack non-

682   uniformity. The results show that the difference between $J_{0.2mm-FEM}$ and $J_{0.2mm-EXP}$ for uniform initial crack

683   configuration is around 6.7%, and around 10.9% for tilted initial crack configuration. Considering the

684   effects of experimental uncertainties, and that many assumptions are introduced in the micromechanical

685   based model, the results are still in an acceptable range.

686   The invalid fatigue pre-crack front in a real mini-CT specimen is much smoother with only one or two points

687   close to the free surface out of the validity limit. As a result, any results obtained from such excessive tilted

688   pre-crack configuration can be considered somewhat exaggerated, and even so, the discrepancy from the

689   uniform pre-crack configuration is only 4.3% (see the results shown in Figure 19-c). This means, in real

690   cases, the critical toughness obtained from the pre-crack configurations that have been identified as

691   invalid according to the current requirements is still meaningful. The current restrictions regarding the

692   pre-crack curvature can be relaxed. Lambrecht et al. [6] proposed that the current validity limit should

693   only take the seven inner measurement points into consideration for the mini-CT specimens tested in the

694   transition range. With minor effects on the fracture toughness results, this new proposal sufficiently

695   decreases the percentage of invalid pre-crack from 8% to 6%. As for the investigations in the ductile regime,

696   applying the validity limit, $\pm0.1\times(b_0B_N)^{1/2}$, on the seven inner points corresponds to the 16.5° tilt angle of

697   this model, which is feasible but, still conservative. Since in this paper, the effect of the 30° tilted pre-crack

698   configuration on $J_{0.2mm}$ is considered to be limited, the corresponding validity limit of ±0.72 mm ($\approx17\%*B$)

699   can be considered when examining the crack size of the seven inner points.

700
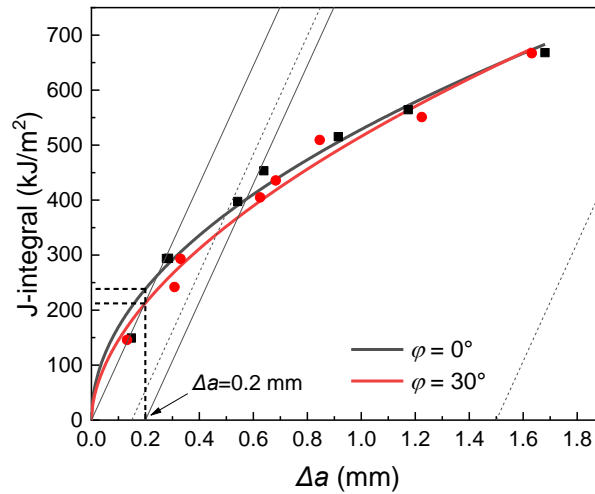
Figure 28 J-R curves (multiple specimen method) of mini-CT specimens with uniform and tilted initial EDM notch

Table 6 Critical toughness values obtained from the mini-CT specimen N96 and N109

T (°C)	Initial crack type	Critical toughness $J_{0.2mm}$ (kJ/m^2)	
		EXP (EDM notch)	FEM (Radius=50 µm)
25	Uniform (φ=0°)	238	223
	Tilted (φ=30°)	213	239

6. Summary and conclusions

For the mini-CT geometry, due to the limited thickness, a non-uniform pre-crack is almost inevitable during fatigue pre-cracking. The existing restrictions in ASTM standards regarding pre-crack size are too strict, resulting in the elimination of a large number of mini-CT specimens, which is believed to be unnecessary. Therefore, efforts were made to investigate the effect of pre-crack non-uniformity on fracture behavior and further discuss the possible relaxation of current restrictions. Prior research have demonstrated very weak influence of non-uniform pre-crack on fracture toughness in the brittle regime. In this paper, comparison of valid uniform pre-crack and invalid non-uniform pre-crack is performed to study the effect of crack non-uniformity on fracture behavior in the ductile regime. The main findings of this paper are:

- Negligible effect (< 3%) of pre-crack non-uniformity on the applied load and global J-integral can be observed, particularly in the range before the initiation of ductile fracture. In contrast, the local properties at the near tip region are redistributed by the non-uniform pre-crack front. The local J-integral and the equivalent plastic strain show larger values near the side with shallow pre-crack, the stress triaxiality shows larger value at the thickness position $x/B_N = 1/4$ (on the shallow crack side of the specimen) and $x/B_N = 1/2$. It is expected that the redistribution will lead to different fracture behavior for the mini-CT specimen with non-uniform pre-crack.

- The micro-mechanical based approach is used to describe fracture initiation. The results are showing that the crack non-uniformity tends to overestimate the critical toughness $J_{0.2mm}$ by 9 kJ/m^2, and slightly shifts the fracture initiation position from mid-thickness to the side with shallower pre-crack. The introduction of the EDM initial crack makes the shift of fracture initiation position more obvious, and increase the deviation of $J_{0.2mm}$ to 16 kJ/m^2.

- The experimental verifications were performed by doing eighteen tests on the mini-CT specimens with uniform ($\varphi = 0°$) and tilted ($\varphi = 30°$) EDM initial notch. The examination of the fracture surface indicates that the crack non-uniformity affects the crack initiation position and subsequent crack propagation characteristics, but the critical initiation load is almost independent of the crack non-uniformity. The experimental data suggest that the applied load in the crack propagation range is reduced due to the inclination of the initial crack, the critical toughness, $J_{0.2mm}$, of the tilted crack configuration is underestimated by 25 kJ/m^2.

Overall, the research conducted on 22NiMoCr37 steel in the present work shows that at room temperature, the crack non-uniformity has a limited effect on the ductile fracture behavior of mini-CT geometry, particularly for the experimental data that are usually being referenced in engineering. Therefore, based on the material and conditions being analyzed, the restrictions in the existing standard ASTM E1820 regarding the fatigue pre-crack curvature can reasonably be relaxed in the ductile regime. The present study suggests that the two outer points of the nine measurement locations can be discarded from the average crack length used for the uniformity criterion, and a new validity limit of ± 0.72 mm (≈17%*B) can be considered in the pre-crack curvature examination.

8. References

[1] R. Chaouadi, E. van Walle, M. Scibetta, and R. Gérard. *On the use of miniaturized CT specimens for fracture toughness characterization of RPV materials*. in *ASME 2016 Pressure Vessels and Piping Conference*. 2016. American Society of Mechanical Engineers, PVP2016-63607.

[2] R. Chaouadi, M. Lambrecht, and R. Gérard. *Crack Resistance Curve Measurement With Miniaturized CT Specimen*. in *ASME 2018 Pressure Vessels and Piping Conference*. 2018. American Society of Mechanical Engineers, PVP2018-84690.

[3] E. Lucon, M. Scibetta, R. Chaouadi, and E. van Walle, *Use of miniaturized compact tension specimens for fracture toughness measurements in the upper shelf regime.* Journal of ASTM International, 2006. **3**(1): p. 1-16.

[4] E. Lucon and M. Scibetta, *Miniature compact tension specimens for upper shelf fracture toughness measurements on RPV steels*, in *Small Specimen Test Techniques: 5th Volume*. 2009, ASTM International.

[5] ASTM, *ASTM E1820-20b*, in *Standard Test Method for Measurement of Fracture Toughness*. 2020, ASTM International: West Conshohocken, PA.

[6] M. Lambrecht, R. Chaouadi, M. Li, I. Uytdenhouwen, and M. Scibetta, *On the Possible Relaxation of the ASTM E1921 and ASTM E1820 Standard Specifications with Respect to the Use of the Mini-CT Specimen.* Materials Performance and Characterization, 2020. **9**(5): p. 593-607.

[7] ASTM, *ASTM E1921-19b*, in *Standard Test Method for Determination of Reference Temperature, T_0, for Ferritic Steels in the Transition Range*. 2020, ASTM International: West Conshohocken, PA.

[8] A. Pineau, A.A. Benzerga, and T. Pardoen, *Failure of metals I: Brittle and ductile fracture.* Acta Materialia, 2016. **107**: p. 424-483.

[9] P. Thomason, *Ductile fracture of metals.* Pergamon Press plc, Ductile Fracture of Metals(UK), 1990, 1990: p. 219.

[10] P. Bridgman, *The stress distribution at the neck of a tension specimen.* Trans. Amer. Soc, 1944.

[11] G. Le Roy, J. Embury, G. Edwards, and M. Ashby, *A model of ductile fracture based on the nucleation and growth of voids.* Acta Metallurgica, 1981. **29**(8): p. 1509-1522.

[12] ASTM, *ASTM E8/E8M-21*, in *Standard Test Methods for Tension Testing of Metallic Materials*. 2021, ASTM International: West Conshohocken, PA.

[13] T.L. Anderson, *Fracture mechanics: fundamentals and applications*. 2017: CRC press.

[14] C. Ruggieri and R.H. Dodds Jr, *An engineering methodology for constraint corrections of elastic–plastic fracture toughness–Part I: A review on probabilistic models and exploration of plastic strain effects.* Engineering Fracture Mechanics, 2015. **134**: p. 368-390.

[15] X. Gao, C. Ruggieri, and R. Dodds, *Calibration of Weibull stress parameters using fracture toughness data.* International Journal of Fracture, 1998. **92**(2): p. 175-200.

[16] T. Pardoen, M. Scibetta, R. Chaouadi, and F. Delannay, *Analysis of the geometry dependence of fracture toughness at cracking initiation by comparison of circumferentially cracked round bars and SENB tests on Copper.* International journal of fracture, 2000. **103**(3): p. 205-225.

[17] C. Ruggieri, R.G. Savioli, and R.H. Dodds Jr, *An engineering methodology for constraint corrections of elastic–plastic fracture toughness–Part II: Effects of specimen geometry and plastic strain on cleavage fracture predictions.* Engineering Fracture Mechanics, 2015. **146**: p. 185-209.

[18] J.P. Petti and R.H. Dodds Jr, *Calibration of the Weibull stress scale parameter, σu, using the Master Curve.* Engineering Fracture Mechanics, 2005. **72**(1): p. 91-120.

[19] J. Koplik and A. Needleman, *Void growth and coalescence in porous plastic solids.* International Journal of Solids and Structures, 1988. **24**(8): p. 835-853.

[20] A. Benzerga, J. Besson, and A. Pineau, *Coalescence-controlled anisotropic ductile fracture.* 1999.

[21] T. Pardoen and J. Hutchinson, *An extended model for void growth and coalescence.* Journal of the Mechanics and Physics of Solids, 2000. **48**(12): p. 2467-2512.

[22] F.A. McClintock, *A criterion for ductile fracture by the growth of holes.* 1968.

[23] J.R. Rice and D.M. Tracey, *On the ductile enlargement of voids in triaxial stress fields∗.* Journal of the Mechanics and Physics of Solids, 1969. **17**(3): p. 201-217.

[24] Y. Huang, *Accurate Dilatation Rates for Spherical Voids in Triaxial Stress Fields.* Journal of Applied Mechanics, 1991. **58**(4): p. 1084-1086.

[25] P. Thomason, *A three-dimensional model for ductile fracture by the growth and coalescence of microvoids.* Acta Metallurgica, 1985. **33**(6): p. 1087-1095.

[26] P. Thomason, *Three-dimensional models for the plastic limit-loads at incipient failure of the intervoid matrix in ductile porous solids.* Acta Metallurgica, 1985. **33**(6): p. 1079-1085.

[27] T.L. Panontin and S.D. Sheppard, *The relationship between constraint and ductile fracture initiation as defined by micromechanical analyses*, in *Fracture Mechanics: 26th Volume*. 1995, ASTM International.

[28] R. Chaouadi, P. De Meester, and M. Scibetta, *Micromechanical modeling of ductile fracture initiation to predict fracture toughness of reactor pressure vessel steels.* Le Journal de Physique IV, 1996. **6**(C6): p. C6-53-C6-64.

[29] J. Hancock and A. Mackenzie, *On the mechanisms of ductile failure in high-strength steels subjected to multi-axial stress-states.* Journal of the Mechanics and Physics of Solids, 1976. **24**(2-3): p. 147-160.

[30] A.M. Kanvinde, *Micromechanical simulation of earthquake-induced fracture in steel structures*. 2004: Stanford University.

[31] M.R. Hill and T.L. Panontin, *Micromechanical modeling of fracture initiation in 7050 aluminum.* Engineering Fracture Mechanics, 2002. **69**(18): p. 2163-2186.

[32] W.-M. Chi, A. Kanvinde, and G. Deierlein, *Prediction of ductile fracture in steel connections using SMCS criterion.* Journal of structural engineering, 2006. **132**(2): p. 171-181.

[33] A. Kanvinde and G. Deierlein, *Void growth model and stress modified critical strain model to predict ductile fracture in structural steels.* JOURNAL OF STRUCTURAL ENGINEERING-NEW YORK-, 2006. **132**(12): p. 1907.

[34] A. Kanvinde, B. Fell, I. Gomez, and M. Roberts, *Predicting fracture in structural fillet welds using traditional and micromechanical fracture models.* Engineering Structures, 2008. **30**(11): p. 3325-3335.